MICROSTRUCTURE AND MAGNETIC PROPERTIES OF COZR AND CO-DOPED TIO2 THIN FILMS

YAO XIAOFENG

NATIONAL UNIVERSITY OF SINGAPORE

2003

MICROSTRUCTURE AND MAGNETIC PROPERTIES OF COZR AND CO-DOPED TIO2 THIN FILMS

YAO XIAOFENG

A THESIS SUBMITTED
FOR THE DEGREE OF MASTER OF ENGINEERING
DEPARTMENT OF ELECTRICAL AND COMPUTER ENGINEERING
NATIONAL UNIVERSITY OF SINGAPORE

2003

Acknowledgement

First, I would like to show my appreciation to National University of Singapore and Data Storage of Institute for providing me this research opportunity and scholarship.

Also, thanks to my project supervisors who give me great help in this work. Special thanks go to Professor Wang Jian-Ping and Dr. Zhou Tiejun for their great patience and enlightening guidance during the course of the entire project. When I meet difficulties, their encouragements help me get rid of the confusion smoothly. And I would like to thank Professor Chong Tow Chong for his support throughout this study.

I wish to express my gratitude to the staff and scholars of Media Materials Group of Data Storage Institute of Singapore. The active discussions throughout the course were extremely beneficial. Special thanks go to Dr Dai Daoyang for the help of TEM and XRD experiments. I also thank Lim Boon Chow and Dr. Branko Tomcik for their great help and support in sputtering system. And thanks to Dr. Sun Chengjun for the fruitful discussion in the microstructure part.

I would also like to acknowledge my thanks to Gai Yaxian in FAC Group of Data Storage Institute for the great help of XPS measurement.

Last but not least, I would like to thank my parents and sister for their constant love and encouragement.

Table of Contents

Chapter 2 Experiment Methods and Characterization Tools 22

Summary

With the fast development of computer technology, magnetic materials play an increasingly important role in the modern society. As the dominant stem of present data storage media, magnetic recording media enter a high developing era with more than 100% growth rate of areal storage density per year. At the same time, the rapid progress of nanotechnology and the raising requirements of electronic devices lead to the novel application of magnetic materials, especially in spintronics.

In this work, two kinds of new magnetic materials were investigated systematically, focusing on the application on data storage and spintronics, respectively. One was CoZr thin film for patterned recording application and the other is Co-doped TiO_2 thin film as a promising candidate for spin injector.

In the first part, microstructure and magnetic properties of CoZr films were investigated in detail, which is for the application of phase transition method to fabricate patterned nanostructures. It is proved that post annealing is effective to induce the phase transition of CoZr thin films from as-deposited non-magnetic state to annealed ferromagnetic state. For $Co_{40}Zr_{60}$ thin films, phase change occurs after annealing at 550°C for 2 hours. The annealing temperature needed for phase change is much lower than that of rapidly quenched bulk samples. $Co_{11}Zr_2$ and $Co_{23}Zr_6$ magnetic phases are formed after annealing, which lead to the enhancement of the magnetism of annealed samples. And, the calculations on Transmission Electron Microscopy-Selected Area Diffraction (TEM-SAD) patterns show that the enlarged grain size may be another source. Moreover, M_s of these two phases were calculated based on Thermomagnetic Analysis (TMA) data. Perpendicular magnetic anisotropy is revealed in annealed samples.

In the second part, Co-doped TiO_2 thin films are studied, which have different layer structures, different Co concentration, and different post-annealing conditions. XPS analysis on the binding state of Co and Ti atoms in the thin films were reported for the first time for this system. Microstructure and magnetic behavior were studied as well. Based on XPS Co2p narrow scan patterns, Co(Ⅱ) binding state is found in most annealed samples, and its intensity increases with the annealing temperature. It is proved that post-annealing is an efficient way to drive Co atoms to diffuse into TiO_2 layers and substitute for Ti in the lattice. It is very interesting to find that samples with partial co-sputtering structure have much stronger Co(Ⅱ) peak in XPS patterns than those of multilayer structure. TEM-SAD patterns show that the annealed films have poly-crystal rutile-TiO_2 phase. Co-fcc phase is not found in annealed films. The low-temperature VSM measurement shows the saturation magnetization at 150 K is 1.325 u_{B} per Co atom, which is close to the value expected for low-spin Co(Ⅱ).

Nomenclature

AFM	Atomic Force Microscope
AGFM	Alternating Gradient Field Magnetometer
Co	Cobalt
Cr	Chromium
d	lattice plane distance
fcc	face centered cubic
Fe	Iron
FWHM	full width half maximum
Gbit/in^2	gigabit per square inch
GMR	giant-magneto resistance
H	magnetic field
H_c	coercivity
hcp	hexagonal close-packed
H_d	demagnetising field
H_{ex}	exchange field
ICP-OES	inductively-coupled-plasma optical-emission-spectroscopy
J	antiferromagnetical coupling constant
K_u	magneto-crystalline anisotropy constant
K_B	Bolzman constant
LAC	Laminated Antiferromagneticallay Coupled
M	magnetization
M_r	remanent magnetization
M_rt	remanence thickness product

M_s	saturation magnetization
MFM	magnetic force microscope
P_{Ar}	Argon gas pressure
S	remanent squareness
S^*	coercive squareness
SNR	signal-to-noise ratio
Tbit/in^2	terabit per square inch
T_{sub}	substrate temperature
TEM	transmission electron microscope
TMA	thermo-magnetic analysis
Ti	Titanium
VSM	vibrating sample magnetometer
XRD	x-ray diffraction
Zr	Zirconium
α	loop slope parameter
δ	film thickness
λ	wavelength of X-ray or electron beam
μ_0	magnetic permeability of vacuum

List of Figures

List of Table

Chapter 1 Introduction

The goal of this introduction chapter is to give a short overview on the applications of magnetic materials on data storage and spintronics. Some basic and important background knowledge will be highlighted.

The story of magnetism begins with a mineral called magnetite (Fe_3O_4), the first magnetic material known to man. In the ancient world the most plentiful deposits of magnetite occurred in the district of Magnesia, in what is now modern Turkey, and our word magnet is derived from a similar Greek word, said to come from the name of this district.

Ferromagnetic material is one of the most important types of magnetic materials. In this material, there are domains in which the magnetic fields of the individual atoms align, but the orientation of the magnetic fields of the domains is random, giving rise to no net magnetic field. When an external magnetic field is applied to them, the magnetic fields of the individual domains tend to line up in the direction of this external field, which causes the external magnetic field to be enhanced.

Magnetic materials have already been widely used in many fields, such as data storage, mechanical and electrical energy conversion, electron control and force application. In recent years, the rapid progress of nanotechnology leads to novel application of magnetic materials in spin electronic devices, magnetic sensors, and functional materials. New magnetic materials are needed, which can meet the high performance requirements of future application. In my work, new magnetic materials on data storage and spintronics have been investigated systematically. The following introduction will focus on these two application fields.

1.1 Application on Data Storage

1.1.1 History of magnetic recording

Magnetic hard disk drives have undergone vast technological improvements since their introduction as storage devices over 45 years ago, and these improvements have had a marked influence on how disk drives are applied and what they can do. Areal density increases have exceeded the traditional semiconductor development trajectory and have yielded higher-capacity, higher-performance, and smaller-form-factor disk drives, enabling desktop and mobile computers to store multi-gigabytes of data easily [1]. Today, when we are familiar with the 1.6 Kg IBM laptop and 40 Gigabits hard disk, it is hard to imagine what the first computer in the world looks like. Within only half of a century, magnetic recording technique grows sharply from zero point to doubling each year of today. (Fig.1.1) As early as 1928, Australia inventor created first magnetic tape, which indicates the beginning of magnetic recording. In 1948, University of California-Berkeley computer project created first magnetic drum to store binary data (800 bits/in^2). 1956 is the most important milestone for magnetic recording, IBM unveiled the RAMAC (Random

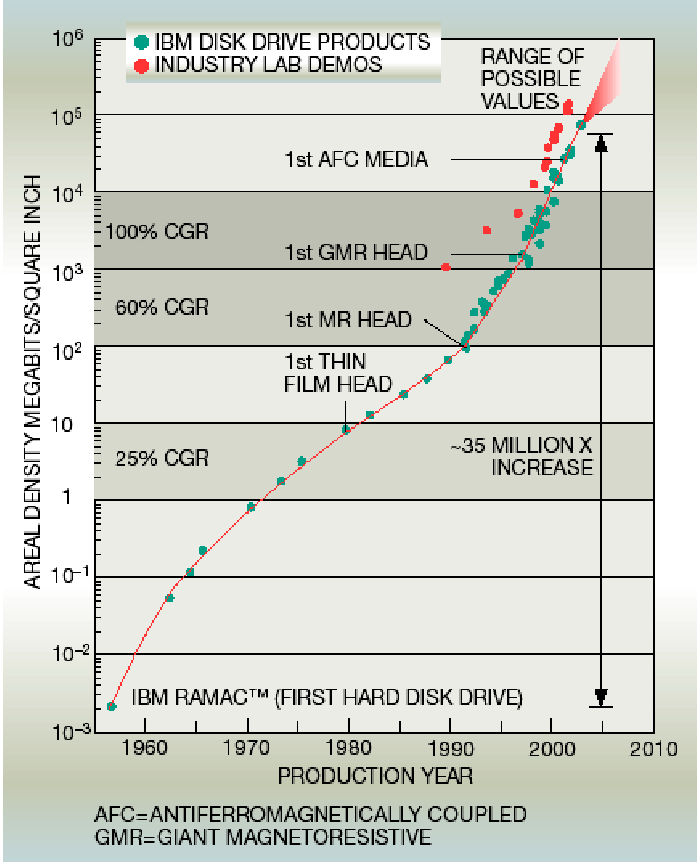

Fig.1.1 Hard Disk Areal Density Trend [1]

Access Method of Accounting and Control), the world's first system for storing computer data on magnetic disks (Fig.1.2). In 1973, the Winchester drives were first introduced. They contained two spindles, each holding 30Mb of data. The Winchester was the first multi-platter drive available and spawned many new technologies. Five years after the Winchester drive was introduced, RAID (Redundant Arrays of Independent Disks) hit the market. This not only sped up data access and allowed more storage, but also introduced the concept of redundancy in computer systems for reliability. By 1987 the University of California at Berkeley had defined the RAID levels still in use today. In the following a few years, the developing step of hard disk was limited by the performance of magnetic head, which was not strong or sensitive enough to detect higher density media. This barrier was broken in 1991. IBM pioneered the use of magnetoresistive (MR) heads for disk drives, which bring an extraordinary increase of areal density (60% per year). Another revolution on hard disk was induced by the use of giant magnetoresistive (GMR), which leaded to Compound Growth Rate (CGR) reach to 100% per year. Hard-disk drive data densities have doubled annually for the past five years, but disk drive designers worried that future progress would be prevented by the impending inability of ever-smaller magnetic-alloy grains to retain their magnetic orientations [5,6]. In 2001, antiferromagnetically coupled (AFC) media was introduced. AFC media makes clever use of three layers to stabilize the magnetic

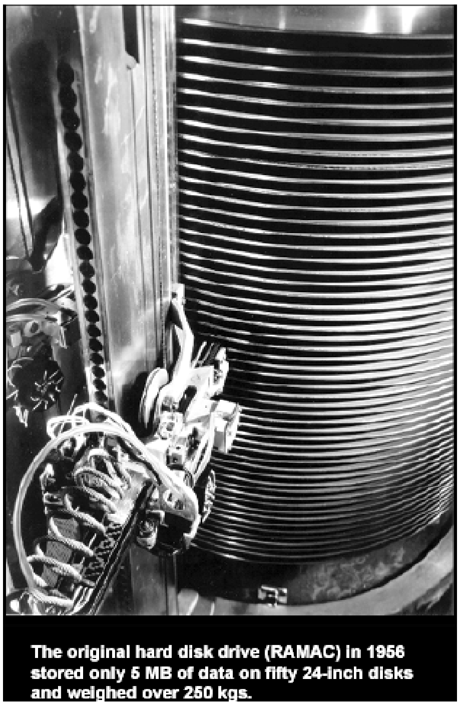

The original hard disk drive (RAMAC) in 1956 stored only 5 MB of data on fifty 24-inch disks and weighed over 250 kgs.

Fig.1.2 RAMAC [1.2]

orientations. With this new design, Fujitsu smashed hard disk recording density record of 106Gb per square inch. Al Hoagland, one of the pioneers on magnetic recording, once said that: “ In my personal time frame, I have witnessed improvement in areal density by a factor of ten million. I can think of no other technology where such dramatic progress could occur over the span of your career.”

1.1.2 Principle of magnetic recording

For magnetic recording, a recording medium and a recording head are needed. Fig.1.3 illustrates the recording process using a single-track ring head. The recording medium consists of a substrate coated with a material that can be permanently magnetized, thus permitting information to be stored magnetically. The recording head is an electromagnet with a gap that has to be located near the medium. The head coil is fed with a current containing the information to be recorded. Upon moving the head at constant speed relative to the medium, the fringing fields from the head gap permanently magnetize the medium and the information is stored. At replay, the medium is again moved past the head and the flux emanating from the medium and entering the head gives rise to a read-back signal. For magneto-resistive read head, the read-back signal comes from the change of the head resistively, which is brought about by the magnetization of the media.

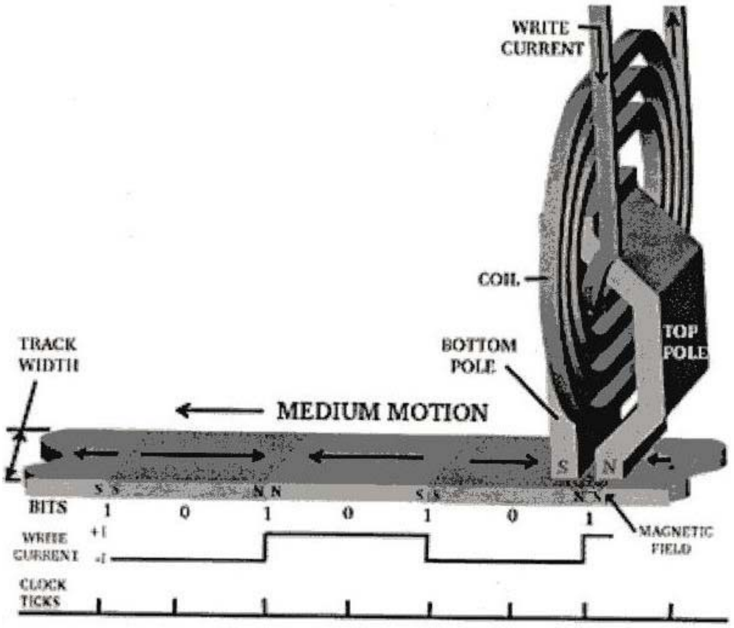

Fig.1.3 Principle of longitudinal magnetic recording[3]

Different modes of magnetic recording exist and can be defined based on the direction of the magnetization or magnetic anisotropy, namely longitudinal magnetic recording (LMR) and perpendicular magnetic recording (PMR). In perpendicular recording, the bits are stored by arranging magnets vertically, with opposite poles facing each other and is therefore more stable at high-storage densities. It is believed that perpendicular recording technology will take over the existing longitudinal technology in the near future. The most popular perpendicular recording media which are widely investigated are Co/Pd multilayers and FePt films. These materials have potential to support densities up to 1 trillion bits per square inch.

In both the longitudinal and perpendicular recording, one bit is stored in a group of many small grains and is therefore thermally unstable. However, in patterned media recording, one bit is stored by one grain and therefore, the grain can be larger (Fig.1.4). Therefore, the integrity of the data can be maintained even at densities higher than 1 trillion bits per square inch.

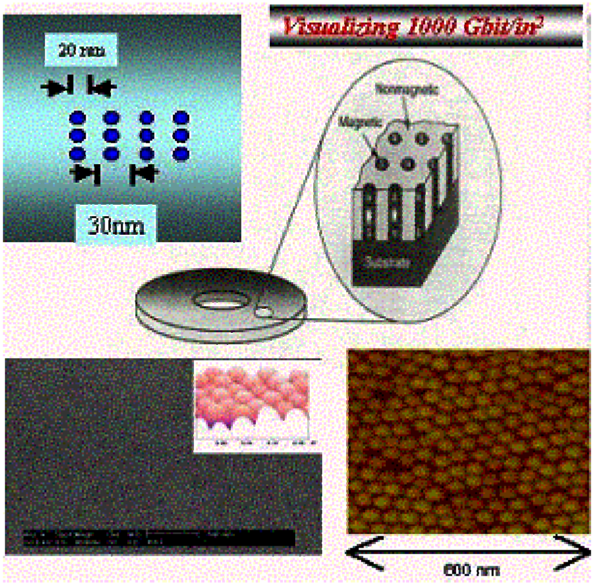

Fig.1.4 Schematic of patterned media and the patterned structure obtained by ion beam bombardment self-assembly. [58]

1.1.3 Magnetic recording media

1.1.3.1 Thin film media

Modern hard disk media incorporate a glass or a NiP-coated aluminum alloy substrate on which a thin film stack is sputtered. The stack consists of one or more underlayers or seed films, a magnetic film, and an overcoat. The magnetic film is a polycrystalline alloy of Co, Cr, and Pt, with additional elements such as B or Ta, and is sputtered at elevated temperatures to promote segregation of non-magnetic elements to the grain boundaries, leading to partial exchange-decoupling of the magnetic grains. Each ~10-nm-diameter grain therefore behaves as a single-domain particle with easy axis parallel to the film plane in longitudinal media (Fig.1.7 b). During the recoding process, small areas of the film (bit cell) are magnetized parallel or antiparallel to the track direction; it is the fringing fields from the magnetization transitions between these areas that are detected by the head during readback [12].

In high-density media, each bit cell contains of order 100 grains. Transition noise, originating from irregularities or jaggedness in the magnetization transitions, and increased by collective reversal of groups of grains, dominates the overall signal-to-noise ratio (SNR) of the system. Both the SNR and the minimum width of the transition depend on the grain size of the medium. As the down-track linear bit density increases, the grain size must decrease to maintain an acceptable SNR. However, the grains begin to exhibit thermal instability when the ratio of thermal

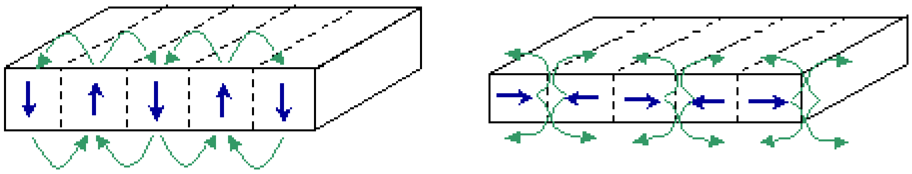

Fig.1.5 Schematic of (a) perpendicular media and (b) longitudinal media

energy kT (k is Boltzmann's constant and T the temperature) to magnetic energy KV (K is the magnetic anisotropy and V the grain volume) exceeds a certain ratio. For isolated grains, stability over a time scale of, for example, 10 years gives a stability criterion of KV/kT > 40, but in a hard disk, the presence of demagnetizing fields at the transition lowers the energy for reversal and increases the required stability ratio.

To increase thermal stability, films with higher values of magnetic anisotropy K could be used, but increases in K are limited by the need for the recording head to produce sufficient field to write the medium. The maximum write field is around 400 kA m^{-1}, leading to a minimum grain diameter of approximately 11-12 nm to ensure thermal stability in CoCrPt-based longitudinal media [15,16]. This is not much smaller than the grains used in current media. Improvements in microstructural uniformity, bit aspect ratio, and signal processing will be necessary to increase areal density further. Several possibilities exist for achieving ultra-high densities. Antiferromagnetically coupled (AFC) media or laminated antiferromagnetically coupled (LAC) media is one way to extend the thermal stability limit in longitudinal media.

Perpendicular media is also an increasingly important alternative, which was first proposed about 20 years ago by Professor Shun-ich Iwasaki [2]. The most outstanding advantage of perpendicular media is its greater thermal stability than that of longitudinal media because the minimization of the demagnetizing fields at extremely high recording density stables the recorded information. Another reason is that the grains can be larger since they can be columns, having a small dimension in plane, important for short bit lengths, while achieving larger volume through greater film thickness. Another merit of perpendicular media involves that sharper transition for higher linear density can be supported on relatively thick media because the demagnetizing field acts to stabilize the transition in perpendicular recording. Thus it is predicted to have higher thermal stability limits, perhaps five times greater than longitudinal media [17,18].

1.1.3.2 Patterned media

Patterned media provide a third concept for extending storage densities to very high values without the need for high write-field. A patterned recording medium, shown schematically in Fig.1.8, consists of a regular array of magnetic elements, each of which has uniaxial magnetic anisotropy. The easy axis can be oriented parallel or perpendicular to the substrate. Unlike the thin film media, the grains within each patterned element are coupled so that the entire element behaves as a single magnetic domain.

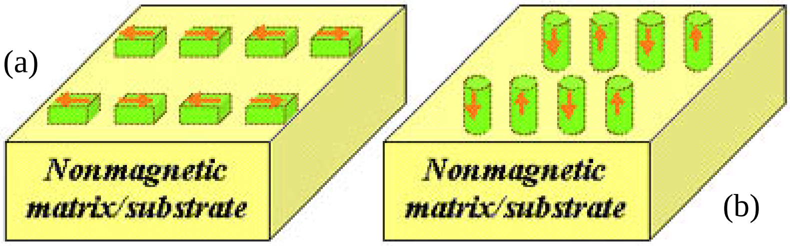

Fig.1.6 Schematic of (a) in-plane and (b) vertical patterned media[59]

The major advantages of such a scheme are first that transition noise is eliminated because that bits are now defined by the physical location of the elements and not by the boundary between two oppositely magnetized regions of a thin film. Second, very high data densities can be obtained because the stability criterion now refers to the volume and anisotropy of the entire magnetic element, not to the individual grains of which it is composed.

At the same time, there are many challenges inherent in patterned media. Most patterned media research has focused on the fabrication and magnetic characterization of media. Fabrication of large-area arrays of elements with dimensions on the sub-50-

nm scale requires advanced lithography or accurate self-assembly techniques. However, these multistep lithography methods involve the cumbersome processes, which greatly complicate the production of patterned magnetic nanostructures. More recently, Zheng et al. [23,24] reported an approach to magnetic patterning by direct laser interference lithography which can produce two-dimensional hexagonal dot arrays with a dot size around 250 nm.

Our group also reported a method of magnetically patterning a non- or weakly magnetic thin film by electron-beam radiation induced nanoscale magnetic phase change, which is also a single-step nanopatterning method [25-27]. Co-C thin films have been investigated and magnetically patterned using this method. The smallest magnetic dot diameter produced by a focused 30 keV electron-beam is about 270 nm. The magnetic dot diameter increases linearly with the square root of explosion time of the radiation per dot, which implies that the magnetic dots are produced by heat-conduction-induced phase change in the film [25]. More suitable magnetic materials are needed for further application, which have phase transition in a short time and with low energy consumption. In the first part of my work, CoZr thin films are studied systematically for the potential application of magnetic nanopatterning via nanoscale magnetic phase change.

1.1.4 Basic magnetic phenomena on magnetic recording

1.1.4.1 Magnetostatic energy and demagnetization energy

It has been long recognized that the magnetostatic field inside a magnetic material is often opposite to the magnetization such that it tends to “demagnetize” the latter. This can be understood by superposing the magnetic field due to point magnetic charges. The magnetostatic field produced by the magnetization itself is called the demagnetizing field [3]. The intensity of the demagnetizing field H_d is proportional to the magnetic free pole density and therefore to the magnetization and the shape of the specimen [4].

1.1.4.2 Magnetic anisotropy

The exchange interaction between spins in ferri- or ferromagnetic materials is the main origin of spontaneous magnetization. This interaction is essentially isotropic, so that the spontaneous magnetization can point in any direction in the crystal without changing the internal energy, if no additional interaction exists. However, in actual ferri- or ferromagnetic materials, the spontaneous magnetization has an easy axis, or several easy axes, along which the magnetization prefers to lie. Rotation of the magnetization away from the easy axis is possible only by applying an external magnetic field. This phenomenon is called magnetic anisotropy [4].

The term magnetic anisotropy is used to describe the dependence of the internal energy on the direction of spontaneous magnetization. We call an energy term of this kind a magnetic anisotropy energy. It is influenced by many factors, including crystal structure, shape, stress and so on. Generally, magnetic anisotropy energy term has the same symmetry as the crystal structure of the material, which is called magnetocrystalline anisotropy [4]. Anisotropy energy is also produced by magnetostatic energy due to magnetic free poles appearing on the outside surface or internal surface of an inhomogeneous magnetic materials. This kind of anisotropy is called shape magnetic anisotropy, which is important in perpendicular media and patterned media.

1.1.4.3 Magnetization reversal mechanism

The Stoner-Wohlfarth theory (model of coherent rotation)

Currently, the grain size of most thin film media is below 20nm in order to achieve high areal density. This dimension is much smaller than the critical size below which only single domain grains form [7].

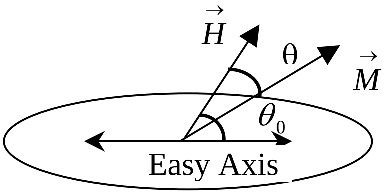

Fig.1.7 Schematic diagram of the Stoner-Wohlfarth model

The Stoner-Wohlfarth theory reveals the hysteresis and reversal mechanism of magnetization in single-domain particles [8]. This model disregards magnetic interactions between grains. The magnetization in these particles is assumed to be always homogenous (model of coherent rotation) and thus applies to elliptical particles only. It was argued that the strong but short-ranged exchange forces are strong enough to always ensure a homogenous magnetization. In order to show a hysteresis, the magnetic material must have a magnetic anisotropy. In shape anisotropy, the magnetization of a single-domain particle seeks to orient itself such that it minimizes magnetostatic energy. In magnetocrystalline anisotropy, the crystal energetically favors certain magnetization orientations. For example, in the case of a material like cobalt with a hexagonal elementary cell, the c-axis is ‘magnetically easy’ and the magnetization likes to point along the c-axis [9]

For a single-domain particle with uniaxial magnetocrystalline anisotropy, the magnetic energy is given by

$$E(\theta) = -\mu_0 M_s H_a V^* \cos\theta + K_u V \sin^2(\theta - \theta_0) \qquad \ldots\text{(eq.1.1)}$$

Where $\mu_0 = 4\pi \times 10^{-7} VsA^{-1}m^{-1}$ is the permeability of free space, M_s is the saturation magnetization, H_a is the applied field, K_u is the (first-order) magnetocrystalline anisotropy constant and V^* is the magnetic switching volume of the particle. θ is the angle between the magnetization and the applied field. θ_0 is the angle between the easy axis and the applied field.

For shape anisotropy, the magnetostatic energy is written as

$$E_M = \frac{1}{2}\ \mu_0 (N_\perp - N_{II}) M_s^2 \qquad \ldots(\text{eq.1.2})$$

This can be described as an anisotropy field where $N_\perp$ and N_{II} are the demagnetizing factors perpendicular and parallel to the easy axis respectively. If the rotational axis of the ellipsoid of revolution coincides with the magnetocrystalline easy axis, the anisotropy energies simply add, i.e. K_u+E_M replaces K_u.

The evaluation of (eq.1.1) yields the magnetic hysteresis loop. The hysteresis loop is determined by finding the energy minima of (eq.1.1), by finding the solution θ_0 to Equation (1.3):

$$\frac{dE}{d\theta_0} = 0 \qquad \ldots(\text{eq.1.3})$$

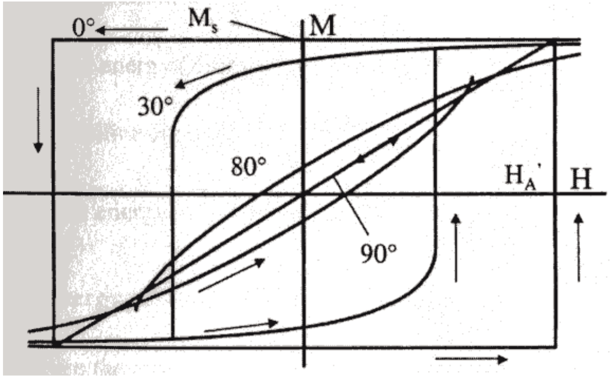

Fig.1.8 H ysteresis curves for a single-domain particle for four angles θ_0 between the easy axis and the applied field. (θ_0=0°, 30°, 80°, 90°)[60]

Fig.1.8 shows the result for θ_0=0°, θ_0=30°, θ_0=80°, θ_0=90°. The Stoner-Wohlfarth model predicts that the coercivity is equal to the effective anisotropy field for θ_0=0°.

For θ_0=90°, the magnetization reversal process is reversible. For the intermediate cases where $0° < \theta_0 < 90°$ the magnetization reveal process consists of both reversible and irreversible processes.

Incoherent magnetization reversal

So far, all calculations assume that the magnetization remains uniform at every instant in these single domain particles. In order to understand more complicated magnetization reversal mechanisms, Brown introduced micromagnetism to describe the process more successfully [1.10,1.11]. In micromagnetic theory, four different energy (density) contributions are considered:

1. magnetic field energy (Zeeman energy) $-\mu \vec{M}_s \vec{H}_a$
2. magnetocrystalline energy
3. magnetostatic energy $-\frac{1}{2}\mu_0 \vec{M}_s \vec{H}_d$
4. exchange energy $A((\nabla m_x)^2 + (\nabla m_y)^2 + (\nabla m_z)^2)$

Where m_x, m_y, m_z are the direction cosines of the magnetization. Also the magnetization reversal process will develop in a way to find the total energy minima.

1.3 Spintronics Applications

1.3.1 Introduction of spintronics

Silicon-based microelectronic devices have revolutionized our world in the past three decades. Each year we see more powerful chips with smaller device features, making them smarter and cheaper. However, the miniaturization of the devices found in integrated circuits is predicted to reach the fundamental physical limits in atomic dimensions [28-30].

According to Muller et al [29], the narrowest feature of present-day integrated circuits is the gate oxide- the thin dielectric layer that forms the basis of field-effect device structures. At the thickness of less than four layers of silicon atoms, current will penetrate through the gate oxide causing the chip to fail [28].

To solve the fundamental physical limits of semiconductor devices, some conceptual revolution in the field of electronics are needed [32], such as “spintronics”. Rather than using electrical fields to manipulate a flow of electrons using their charge as a handle, spintronics marshals electrons through their spin. The advantages of these new devices would be nonvolatility, increased data processing speed, decreased electric power consumption, and increased integration densities compared with conventional semiconductor devices.

1.3.2 GMR effect

This discovery in 1988 of the giant magnetoresistive effect (GMR) is considered the beginning of the new, spin-based electronics [35,36]. GMR is a quantum mechanical effect observed in layered magnetic thin film structures that are composed of alternating layers of ferromagnetic and nonmagnetic layers. When the magnetic moments of the ferromagnetic layers are parallel, the spin-dependent scattering of the carriers is minimized, and the material has its lowest resistance. When the ferromagnetic layers are antialigned, the spin-dependent scattering of the carriers is maximized, and the material has its highest resistance. The directions of the magnetic moments are manipulated by external magnetic fields that are applied to the materials. These materials can now be fabricated to produce significant changes in resistance in response to relatively small magnetic fields and to operate at room temperature [34].

1.3.3 Spin valve in magnetic recording

The first application to produce a substantially large economic impact was that for the read heads in magnetic disk recorders. Spin valve, a GMR-based device, is the key component of read head. A spin valve has two ferromagnetic layers (alloys of nickel, iron, and cobalt) sandwiching a thin nonmagnetic metal (usually copper), with one of the two magnetic layers being “pinned”; i.e., the magnetization in that layer is relatively insensitive to moderate magnetic fields [37]. The other magnetic layer is called the “free” layer, and its magnetization can be changed by application of a relatively small magnetic field. As the magnetizations in the two layers change from parallel to antiparallel alignment, the resistance of the spin valve rises typically from 5 to 10%.

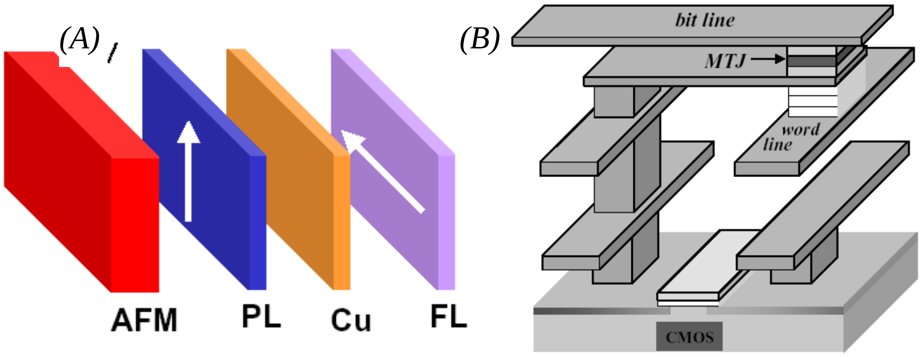

Fig.1.9 Spin-dependent transport structures:
(A) spin valve, (B) Magnetic RAM (MRAM)

1.3.4 Magnetic tunnel junction in nonvolatile memories

A magnetic tunnel junction (MTJ) is a device in which a pinned layer and a free layer are separated by a very thin insulating layer, commonly aluminum oxide [38,39]. The tunneling resistance is modulated by magnetic field in the same way as the resistance of a spin valve is, exhibits 20 to 40% change in the magnetoresistance. Applications for GMR and MTJ structures are expanding, and one of the important applications is magnetoresistive random access memory (MRAM). MRAM uses magnetic hysteresis to store data and magnetoresistance to read data. GMR-based MTJ or pseudospin valve memory cells are integrated on an integrated circuit chip and function like a static semiconductor RAM chip with the added feature that the data are retained with power off. Potential advantages of the MRAM compared with silicon electrically erasable programmable read-only memory (EEPROM) and flash memory are 1000 times faster write times, and lower energy for writing. MRAM data access times are about 1/10,000 that of hard disk drives.

1.3.5 Quantum computation in the future

The idea of a quantum computer has been developed theoretically over several decades to elucidate fundamental questions concerning the capabilities and limitations of machines in which information is treated quantum mechanically [40,41]. Specifically, in quantum computers the ones and zeros of classical digital computers are replaced by the quantum state of a two-level system (a qubit).

The states of spin ½ particles are two-level systems that can potentially be used for quantum computation. Nuclear spins have been incorporated into several quantum computer proposals because they are extremely well isolated from their environment and so operations on nuclear spin qubits could have low error rates. The primary challenge in using nuclear spins in quantum computers lies in measuring the spins. A possible approach is to incorporate nuclear spins into an electronic device and to detect the spins and control their interactions electronically. Electron and nuclear spins are coupled by the hyperfine interaction [41]. Under appropriate circumstances, polarization is transferred between the two spin systems and nuclear spin polarization is detectable by its effect on the electronic properties of a sample.

1.3.6 Materials for spintronics application

Ferromagnetic semiconductor (FS) obtained by doping magnetic impurities into host semiconductors are key materials for spintronics in which the correlation between charge and spin of electrons is used to bring about spin-dependent electronic functionality such as giant magnetoresistance and spin field effect transistor [42]. There are three classes of FS materials, Ⅲ-Ⅴ compounds, Ⅱ-Ⅵ compounds and transitional metal doped TiO_2. It has recently been shown that Mn/Be-doped and Mn-doped ZnSe can be grown epitaxially on $GaAs/Al_xGa_{1-x}As$ quantum-well structure and used to achieve at least 50% spin injection efficiency into the quantum well. However, a major drawback of conventional Ⅲ-Ⅴ and Ⅱ-Ⅵ semiconductors doped with magnetic transition metal ions is that the measured Curie points are well below room temperature [45].

In contrast, Co-doped TiO_2 anatase has very recently been demonstrated to be weakly ferromagnetic and semiconducting for doping levels up to ~8 at.%, and temperatures of up to 400 K [45]. For large-scale application at room-temperature, Co-doped TiO_2 thin film is one of the promising candidates. In the second part of this work, we are focused on Co-doped TiO_2 system, and a detailed literature review are reported in chapter 4.

Reference:

[1] E. Grochowski, R.D. Halem, *IBM Systems Journal*, Vol.**42**, No.2, 2003

[2] http://www.iist.scu.edu/

[3] Shan X. Wang, Alexander M. Taratoril, “*Magnetic Information Storage Technology*”, p16, Boston: Academic Press, 1998

[4] Soshin Chikazumi, C.D. Graham, JR, “*Physics of Ferromagnetism*”, p249, Oxford: University Press, 1997

[5] P.L.Lu, S.H.Charap, *IEEE Trans. Magn*. **31**, 2767 (1995)

[6] Dieter Weller, Andreas Moser, *IEEE Trans. Magn.***35**, 4423 (1999)

[7] J.C. Mallinson, “*The Foundations of Magnetic Recording*” (2nd edition), Boston: Academic Press, (1993)

[8] E.C. Stoner, E.P. Wohlfarth, *Phil. Trans. R. Soc*. **A240**, p599 (1948)

[9] T.C. Arnoldussen, “Film Media” in “*Magnetic Recording Technology*”, p165-230, McGraw-Hill/Mee 83-Z, (1988)

[10] W.F. Brown Jr, “Virtues and weaknesses of the domain concept”, *Rev. Mod. Phys*. **17**, 15-19 (1945)

[11] W.F. Brown Jr, “*Micromagnetics*”, Huntington: Krieger (1978)

[12] C.A. Ross, Annu. *Rev. Mater. Res*. **31**, 203 (2001)

[13] S.Y. Chou, *Proceedings of the IEEE* **85**, 652 (1997)

[14] N. Helian, F.Z. Wang, W.W. Clegg, *J. Magn. Magn. Mater*. **233**, 305 (2001)

[15] D. Weller, M. Doerner, Annu. *Rev. Mater. Sci*. **30**, 611 (2000)

[16] H.N. Bertram, H. Zhou, R. Gustafson, *IEEE Trans. Magn*. **34**, 1845 (1998)

[17] K. Ouchi, N. Honda, *IEEE Trans. Magn*. **36**, 16 (2000)

[18] H.N. Bertram, M. Williams, *IEEE Trans. Magn*. **36**, 4 (2001)

[19] R. Wood, *IEEE Tran. Magn*. **36**, 36 (2000)

[20] H. Katayama, S. Sawamura, Y. Ogimoto, K. Kojima, K. Ohta, *J. Magn. Soc. Jpn.* **23**, 233 (1999)

[21] H. katayama, M. Hamamoto, J. Sato, Y. Murakami, K. Kojima, *IEEE Trans. Magn.* **36**, 195 (2000)

[22] S. Iwasaki, and K. Takemura, *IEEE Trans. Magn*. Vol. MAG-11, No.5, 1173 (1975)

[23] M. Zheng, M. Yu, Y. Liu, R. Skomski, et al. *IEEE Trans. Magn*. **37**, 2070 (2001)

[24] M. Zheng, M. Yu, Y. Liu, R. Skomski, et al. *Appl. Phys. Lett*. **79**, 2606 (2001)

[25] T.J. Zhou, Y. Zhao, J.P. Wang, J.T.L. Thong, and T.C. Chong, *IEEE Trans. Magn.* **38**, 1970 (2002)

[26] T.J. Zhou, Y. Zhao, J.P. Wang, J.T.L. Thong, and T.C. Chong, *J. Appl. Phys*. **91**, 8019 (2002)

[27] Y. Zhao, T.J. Zhou, J.P. Wang, J.T.L. Thong, X.F. Yao, and T.C. Chong, *J. Appl. Phys.* **93**, 7417 (2003)

[28] Max Schulz, *Nature* **399**,729-730 (June 24th,1999)

[29] Muller, T.Sorsch, et al., *Nature* **399**,758-761 (June 24th, 1999)

[30] T. Dietl, H. Ohno, F. Matsukura, J. Cibert, and D. Ferrand, *Science* **287**, 1019 (2000)

[31] Gary A. Prinz, *Science* **282**, 1660 (1998)

[32] News feature, *Nature* **404**, 918 (2000)

[33] S.A. Wolf, D.D. Awschalom, R.A. Buhrman, et al., *Science* **294**, 1488 (2001)

[34] D.A. Muller, T. Sorsch, S. Moccio, F.H. Baumann, K. Evans-Lutterodt, and D. Timp, *Nature* **399**, 758 (1999)

[35] M. Baibich et al., *Phys. Rev. Lett.* **61**, 2472 (1988)

[36] J. Barnas, A. Fuss, R. Camley, P. Grunberg, W. Zinn, *Phys. Rev. B.* **42**, 8110 (1990)

[37] B. Dieny et al., *J. Appl. Phys.* **69**, 4774 (1991)

[38] J.S. Moodera, L.R. Kinder, T.M. Wong, R. Meservey, *Phys. Rev. Lett.* **74**, 3273 (1995)

[39] T. Miyazaki et al., *J. Magn. Magn. Mater.* **151**, 403 (1995)

[40] Loss, D. & DiVincenzo, D. P. Quantum computation with quantum dots. *Phys. Rev. A* **57,** 120–126 (1998)

[41] Privman, V., Vagner, I. D. & Kventsel, G. Quantum computation in quantum Hall systems. *Phys. Lett. A* **239,** 141–146 (1998).

[42] Y. Matsumoto, M. Murakami, T. Shono, et al., *Science* **291**, 854 (2001)

[43] Y. Matsumoto, M. Murakami, Z. Jin, et. al, *Jpn. J. Appl. Phys.* **38**, L603 (1999)

[44] Y. Matsumoto, M. Murakami, T. Hasegawa, et al., *Appl. Surf. Sci.* **189**, 344 (2002)

[45] S.A. Chambers, S. Thevuthasan, et al., *Appl. Phys. Lett.* **79**, 3467 (2001)

[46] S.A. Chambers, T. Droubay, C.M. Wang, et al., *Appl. Phys. Lett.* **82**, 1257 (2003)

[47] S. A. Chambers, S. M. Heald, and T. Droubay, *Phys. Rev. B* **67**, 100401® (2003)

[48] W.K. Park, R.J. Ortega-Hertogs, J.S. Moodera, A. Punnoose, and M.S. Seehra, *J. Appl. Phys.* **91**, 8093 (2002)

[49] B.Z. Rameev, F. Yildiz, L.R. Tagirov, B. Aktas, et. al, *J. Magn. Magn. Mater.* **258-259**, 361 (2003)

[50] P.A Stampe, R.J. Kennedy, Y. Xin, J.S. Parker, *J. Appl. Phys*. **92**, 7114 (2002)

[51] D.H. Kim, J.S. Yang, K.W. Lee, S.D. Bu, et al., *Appl. Phys. Lett*. **81**, 2421 (2002)

[52] J.S. Yang, D.H. Kim, S.D. Bu, T.W. Noh, et al., *Appl. Phys. Lett*. **82**, 3080 (2003)

[53] J.-Y. Kim, J.-H. Park, B.-G. Park, et al., *Phys. Rev. Lett*. **90**, 017401-1 (2003)

[54] Y.L. Soo, G. Kioseoglou, S. Kim, Y.H. Kao, et al., *Appl. Phys. Lett*. **81**, 655 (2002)

[55] I.-B. Shim, S.-Y. An, C.S. Kim, S.-Y. Choi, Y.W. Park, *J. Appl. Phys*. **91**, 7914 (2002)

[56] S.A. Chambers, *Mat. Today* **5**, 34 (2002)

[57] S.A. Chambers, C.M. Wang, S. Thevuthasan, T. Droubay, et al., *Thin Solid Films* **418**, 197 (2002)

[58] J.L. Sullivan, W. Yu and S.O. Saied, *Surf. Interf. Anal.* **22,** 515 (1994)

[59] Shan X. Wang, Alexander M. Taratoril, *“Magnetic Information Storage Technology”*, p198, Boston: Academic Press, (1998)

[60] B.D. Cullity, *“Introduction to Magnetic Materials”*, p336, Addison-Wesley Publishing Company, (1972)

Chapter 2 Experiment Methods and Characterization Tools

This chapter mainly covers the sample preparation techniques, i.e., sputtering technique, and the measurement methods used in the project.

2.1 Thin film deposition: magnetron sputtering

Sputtering deposition is a kind of physical-vapor deposition (PVD) techniques, which is being widely used for thin film fabrication. It allows a wide selection of materials and produces films with high purity, great adhesion, good uniformity and homogeneity at economic cost. Sputtering is the preferred method used to deposit all the different layers (except lubricant) in rigid-disk nowadays. The main reason for this is the capability to precisely control the sputtering parameters such as sputtering gas pressure, sputtering power density, bias voltage, and substrate temperature which play very important roles in defining the thin film microstructure and other properties. Careful manipulation of these variables is critical to achieve the desired magnetic properties and microstructure of the thin films prepared [1]

2.1.1 Principle of Sputtering

The sputtering process is the ejection of surface atoms or molecules of a solid or liquid due to the momentum transfer associated with surface bombardment by energetic particles such as argon ions. The ejected atoms or molecules then condense on a substrate to form a thin film. A schematic diagram of a typical planer DC-diode sputtering system is shown in Fig.2.1. Sputtering is performed in a vacuum chamber, which has been pumped down by a series of mechanical and high vacuum pump, to a pressure below

5×10^{-7} Torr. The chamber is then backfilled with a sputtering gas to a pressure of militorr range so as to provide a suitable medium in which a glow discharge can be initiated and maintained to continuously supply the bombarding particles. Argon gas is generally used because its large atomic mass led to good sputtering yield as well as its low cost. The target composed of the material to be deposited, is placed into the vacuum chamber together with substrates. The substrates are usually placed in front of the target. The target is connected to a negative voltage supply, which can be either DC or RF. The substrates can be grounded, floating, biases or heated [1,2].

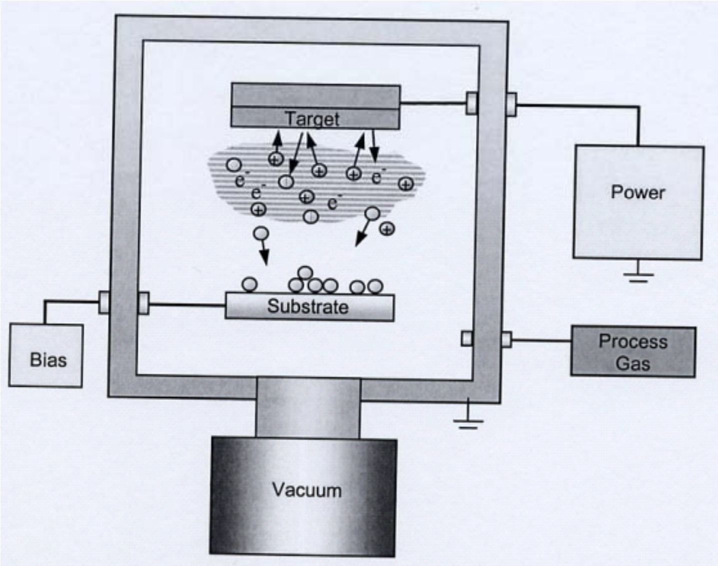

Fig.2.1 Schematic depiction of a typical sputtering system [8]

The sputtering process is initiated by applying a negative potential to the target. When the voltage exceeds a threshold value, stable glow discharge appears. In the presence of negative potential, free electrons are accelerated and ionized the argon gas atoms. A mixture of positively charged argon ions and negatively charged electrons, or plasma is thus formed in between the target and the substrate. The target with a negative potential attracted the positive argon ions. The argon ions accelerated towards the target and bombarded the target surface with a relatively high energy. The sputtering atoms fly off in random directions, and some of them land on the substrate, condense there, and form a thin film layer. The energy of these atoms generally follows a cosine distribution [2,3]. The atoms need to travel through the plasma in between the target and substrate before arriving at the substrate surface, during which, there may be collision between the neutral atoms, argon ions and other particles described above.

Magnetron sputtering has been introduced to increase sputtering rate since 1970. In general, magnetron sputtering systems can be defined as diode devices in which magnetic fields are used together with the cathode surface to form electron traps [3]. A magnetic field in the form of a racetrack is formed on the target by placing magnets on the back of the target as shown in Fig. 2.2. The magnetic field causes the electrons to follow a longer helical path near the target surface thus increasing the ionization of the argon gas. This allows lower pressures and voltages to be used while achieving high deposition rate.

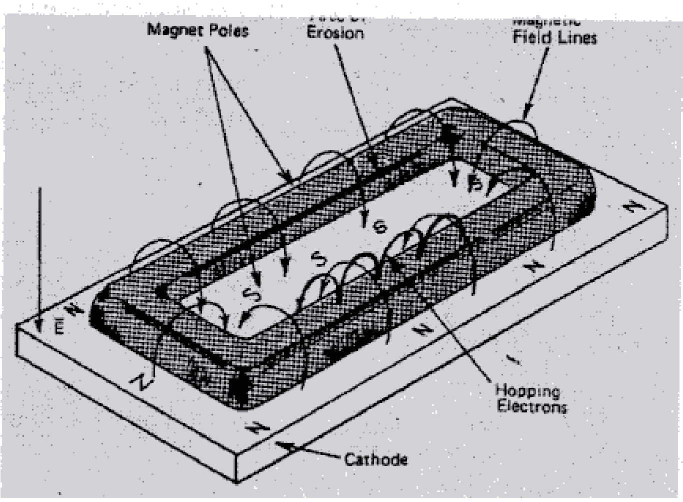

Fig. 2.2 Schematic diagram of the principle of Magnetron Sputtering Method [7]

There is an advantage in the sense that most of the secondary electrons are concentrated near the target. These electrons do not interact with the substrate, thus resulting in a reasonable low substrate temperature since secondary electrons are responsible for 80% of the heat flux to the substrate. A further advantage is the higher deposition rate and a more efficient use of the target material by an optimal arrangement of the magnets.

2.1.2 Working Pressure

The pressure selected for the argon gas dictates the speed as well as the movement of particles and hence affects the microstructure of the films deposited. A low argon gas pressure will result in low sputtering yield/rate since the sputtering process involves the bombardment of working gas ions on the target surface of the materials to be deposited. The sputtering yield will increase as the pressure increase since more argon ions will be bombarding the target surface due to an increase ionization probability of argon gas. On the other hand, the sputtering atoms will reach the substrate at a higher energy for a constant power density applied at low pressure. The energy of these atoms will be reduced if higher pressure is used. This is because the sputtered atoms need to travel through the glow discharge region before arrive at the substrate surface, these atoms will come into collision with the argon atoms, ions and electrons, losing some of its energy to the collision.

The effect on the film structure of the sputtering parameters was summarized by the Thornton Zone Diagram (Fig.2.3), which was derived from studies of thick metal films but can be used as a guide to the growth of all films. The diagram has different zones; the structure changes from one zone to another if either argon pressure decreases or substrate temperature increases which both increase the adatoms mobility on the substrate surface.

2.1.3 Substrate Temperature

Substrate temperature plays an important role in the growth of thin films such that a higher substrate temperature fosters higher mobility of adatoms, which also promotes inter-grain diffusion. This decouples the grains during the film deposition, which corresponds to zone T to zone 2 of the Thornton zone diagram where internal diffusion can take place. However, when substrate temperature exceeds a certain value, lattice diffusion dominates, giving rise to the large, equiaxed recrystallized grains of zone 3.

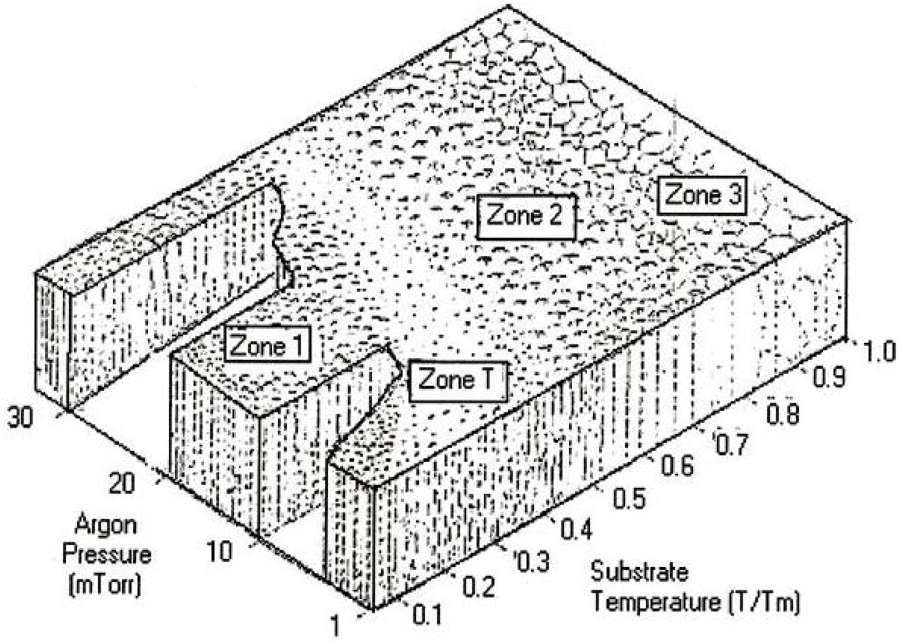

Fig.2.3 Thornton zone diagram showing thin film microstructure as a function of Ar pressure and substrate temperature [6].

2.1.4 Sputtering Power Density

The power applied to the target determines the energy level of the argon ions bombarding the target surface and hence the energy of the sputtered atoms. At high power density, the adatoms arrive at the substrate with high energy level that translate into high adatom mobility, which promotes dense and small columnar grains. However, adatoms arriving later at the substrate with very high energy may bombard the deposited film causing the film to be resputtered and sometimes induce defect on the film. Therefore, the power density used to prepare the samples needs to be carefully selected in order to achieve the desired film properties.

2.2 Post-annealing process

Post-annealing process is performed on the prepared samples using a vacuum furnace in the Media Laboratory of Data Storage Institute. The samples are first placed on a stainless steel tray and put into the center of the ceramic tube of the furnace. A vacuum better than 5×10^{-4} Torr is achieved using a molecular pump, after pumping for more than one hour. The temperature is raised to and maintained at the setting value. After that the heater is turned off and the samples are left to cool down naturally which normally takes more than 5 hours.

2.3 Vibrating Sample Magnetometer (VSM)

The vibrating sample magnetometer (VSM) is the most commonly used instrument in the characterization of magnetic thin film media. From these measurements, macromagnetic properties such as saturation magnetization, remnant magnetization, coercive force, squareness, permeability, and etc. can be determined.

The principle of VSM is based on the Faraday's Law of Electromagnetic Induction that states that the voltage induced in an electrical circuit is proportional to the rate of change of magnetic flux linking the circuit [4]. It employs an electromagnet that provides the DC magnetizing field, a vibrator mechanism to vibrate the sample in the magnetic field, and detection coils, which generate the signal voltage due to the changing flux emanating from the vibrating sample. The output of measurement displays the magnetic moment M as a function of the field H.

For DMS 1660 VSM (digital measurement system) as shown in Fig.2.4, which is used in our lab, a maximum field of 20,000 Oe can be achieved, so as to give a magnetic field resolution at 1 Oe at 32K Oe range and a magnetic moment sensitivity of 1×10^{-5} emu.

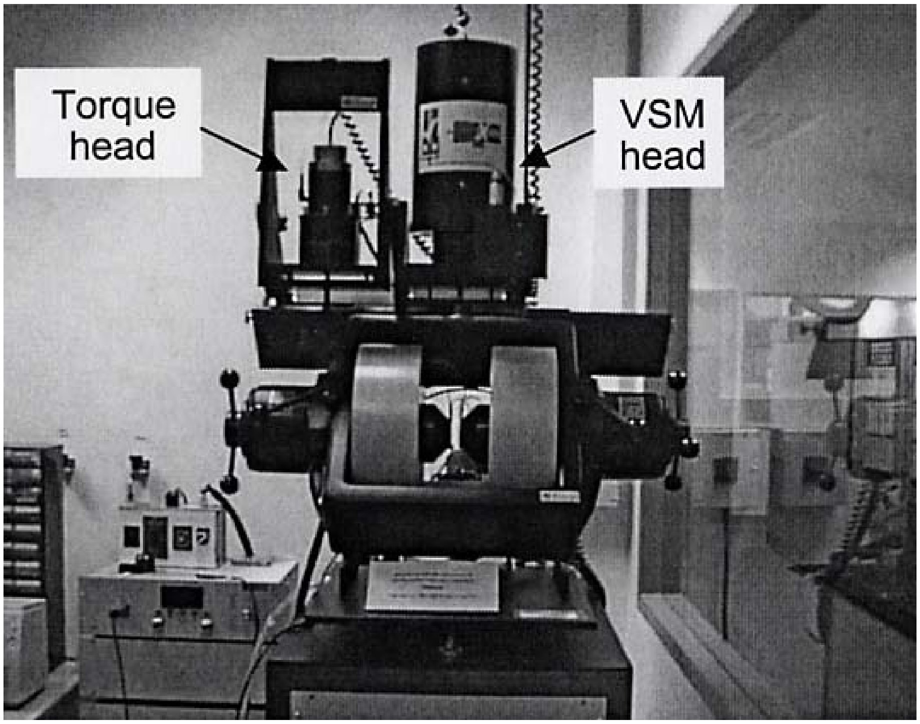

Fig. 2.4 Photograph of Vibrating Sample Magnetometer (DMS 1660)

How the sample is placed between the electromagnet pair will give the magnetic measurement at different direction. When the sample plane is parallel with the magnetic field, the in-plane magnetic properties will be measured. When the sample plane is making a 90º angle with the magnetic field, the magnetic properties in the perpendicular direction will be measured.

2.4 Alternating Gradient Force Magnetometer (AGFM)

The Alternating Gradient Force Magnetometer has enjoyed significant acceptance in present-day magnetic metrology because of its high sensitivity. The AGFM has a noise floor of 10^{-8} emu compared with 10^{-6} emu for the VSM. In an AGFM, as shown in Fig. 2.5, the sample is mounted on an extension rod attached to a piezoelectric element. An alternating gradient field produces a periodic force on a sample placed in a DC field of an electromagnet. The alternating field gradient exerts an alternating force on the sample, proportional to the magnitude of the gradient field, the magnetic moment of the sample and the intensity of the applied field. The resulting deflection of the extension is transmitted to the piezoelectric sensing element. The output signal from the piezoelectric element is synchronously detected at the operating frequency of the gradient field. The signal developed by the piezoelectric element is greatly enhanced by operating at or near the mechanical resonant frequency of the sample assembly.

The AGFM in use in the Media Laboratory of DSI is the Model 2900 MicroMag^{TM} System from Princeton measurement. Sensitivity in the order 10^{-8} can be achieved. The maximum field of 2.5 kOe can be produced.

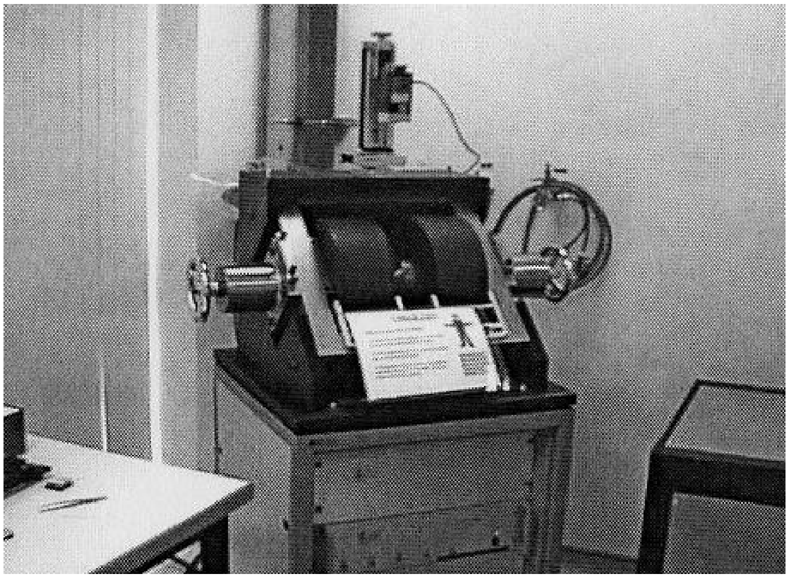

Fig. 2.5 Photograph of Alternating Gradient Force Magnetometer

2.5 X-Ray Diffractometer (XRD)

X-ray diffraction is a versatile, non-destructive analytical technique for identification and quantitative determination of the phase composition of crystalline and amorphous materials. The measurement results provide direct information on the atomic-level spacing of crystal planes within the lattice of the sample. The X-ray diffractometer can distinguish between crystal structures with identical compositions. Other information like the amount of atomic ordering present in the crystal can also be determined.

The crystal lattice is a regular three-dimensional distribution of atoms in space. These are arranged so that they form a series of parallel planes separated from one another by a distance d, which varies according to the nature of the material. For any crystal, planes exist in a number of different orientations-each with its own specific d-spacing. When a monochromatic X-ray beam is projected onto a crystalline material at an angle θ, diffraction occurs only when the distance traveled by the rays reflected from successive planes differs by a complete number n of wavelengths, which describes by the Bragg's Law, which reads:

$$n\lambda = 2d\sin\theta \qquad \text{(Eq.2.1)}$$

By varying the angle θ, the Bragg's Law conditions are satisfied by different d-spacing in polycrystalline materials. Plotting the angular positions and intensities of the resultant diffracted peaks of radiation produces a pattern, which is characteristic of the sample.

The model we use for X-ray diffraction is Philips X'pert MRD. The general configuration of the XRD system is shown in Fig.2.6

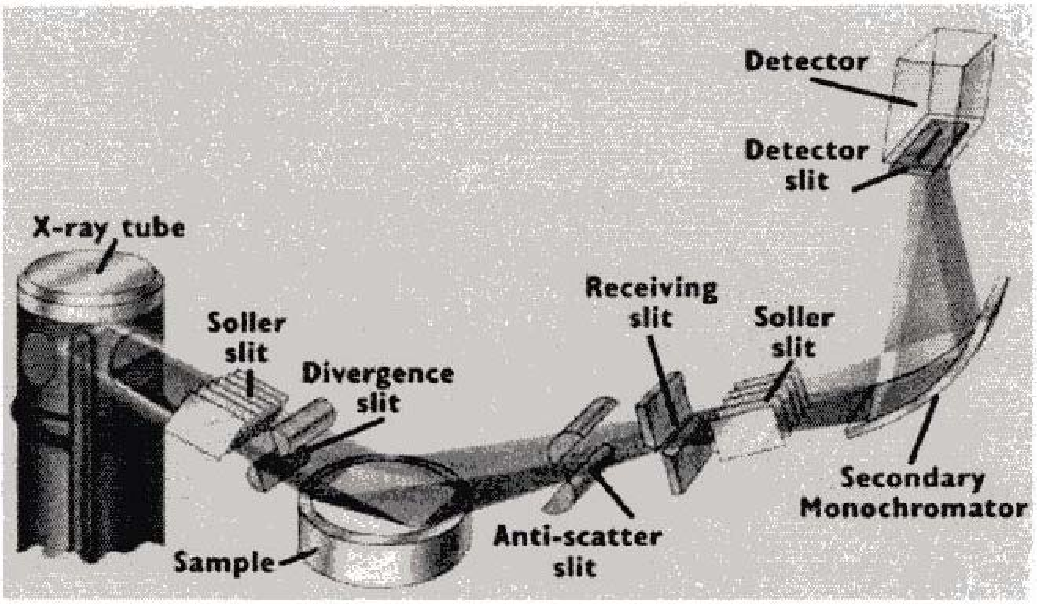

Fig.2.6 General configuration of Philip's X'pert XRD system

2.6 Transmission Electron Microscope (TEM)

Transmission electron microscope is a very useful for material research. It is mainly used to get the information of microstructure and orientation of crystals as well as its chemical composition.

2.6.1 Principle of TEM

The ultimate resolution of any imaging technique is limited by the wavelength of the radiation that carries the information. Thus, in order to image individual atomic positions in crystals, namely get a resolution of about 0.1 nm, the radiation with much smaller wavelength than light (the wavelength of light is on the order of 500 nm) is needed. As we know, all moving objects are associated with a wavelength, given by De Broglie relationship:

$$\lambda = \eta / \rho \qquad \text{(Eq.2.2)}$$

where $\lambda$is the wavelength,$\eta$is Planck's constant, and ρ is the momentum of the object. For a electron moving in an accelerating electrical field, Eq(2.2) comes to[5]:

$$\lambda(nm) = 0.1 \times (150 / V)^{1/2} \qquad \text{(Eq.2.3)}$$

where V is the accelerating voltage. Hence, λ decreases as the accelerating voltage increases. For electrons accelerated by V=100 kV, λ is 3.7 pm which is shorter by a factor of 10^5 than visible light. Such electrons are capable of carrying information at very high resolution through a specially designed instrument. Since they can travel significant distances through matter (typically on the order of tens of nanometers), they are able to probe the microstructure of materials.

2.6.2 Basic Layout of TEM

Usually, there are five fundamental parts in TEM including source of illumination (electron gun), condenser system, objective lens, projector system and image capture system (screen and camera). The function of the electron gun is to produce an intense beam of electrons through thermo-ionic emission or field emission. Three parameters can be used to control the quantity and energy of electrons. They are filament current, grid bias, and accelerating voltage. The condenser system in TEM controls how strongly the beam is focused onto the specimen by spreading it to illuminate a larger or a smaller area. The condenser system only provides slight magnification and it is equipped with an aperture to improve the image contrast. The objective lens is the most important component in TEM. It is used for focusing image and it contributes most to the image magnification. Projector system, consisting of four lenses, determines the magnification of the microscope. Two operating modes, image mode and diffraction pattern mode, can be achieved by controlling projector system.

The model of our TEM is HITACHI-8100. Its maximum accelerating voltage is 200 kV. Its magnification is up to $10^6\times$ for zoom mode and selected area mode. Its resolutions are 1.44 $\overset{\circ}{A}$ for lattice image and 2.1 $\overset{\circ}{A}$ for point to point, respectively.

2.6.3 TEM Sample Preparation

The purpose of sample preparation is to get thin enough samples that the accelerated electrons can transmit through them. There are two kinds of sample preparation; one is plain-view sample preparation and the other is cross-section sample preparation. To get qualified samples whose thin area thickness is less than 100 nm, great patience and carefulness are needed. Sample preparation basically can be completed after four steps. First step is cutting, following is grinding to a uniform thickness of about 0.3 mm, then dimpling a hollow in the central uniform and the last step is ion milling to get desired thin area. Every step is very important for the final result.

2.6.4 TEM Images

Generally, there are three kinds of images of TEM samples. They are Bright Field Image, Dark Field Image and Diffraction Pattern Image.

Bright Field Images are produced when the objective aperture prevents the diffracted beam from passing and contributing to the image. Hence, when a sample with crystalline structure is placed in the beam in front of the lens, it is possible that in some areas electrons are diffracted from the incident beam into other directions. These diffracted electrons are taken from the direct beam, which is therefore locally reduced in intensity. Since only the directly transmitted electrons contribute to the image, the areas where diffraction is occurring appear dark.

Dark Field Microscopy is obtained when the incident beam is tilted in such a way that a diffracted beam of interest passes through the lens on the optical axis, and hence through the objective aperture. This technique is called Dark Field Microscopy because holes in the sample are dark in the image. The contrast in dark-field images can be extremely high, enhancing the visibility of weak features.

Diffraction Pattern Image is generated only when the TEM sample is of crystalline structure. Electrons employed for transmission microscopy have a wavelength on the order of a few picometers. A typical interplanar spacing for densely packed planes in most crystals is about 0.2 nm. Similarly with X-ray diffraction, TEM diffraction only occurs when the Bragg’s Law (Eq. 2.1) is obeyed. The difference between these two diffraction measurements is the different detected lattice planes. In X-ray diffraction, the measured series planes are parallel to the sample surface, while in TEM diffraction, they are perpendicular to the sample surface.

2.7 Energy Dispersive X-Ray Microanalysis (EDX)

Our TEM HITACHI-8100 is equipped with an Oxford-Links EDX. When a thin section of a specimen of interest is irradiated by a fine probe of electrons, the interaction of the electrons and the atoms of the specimen results in the generation of the X-rays whose energy is characteristic of the atoms which emitted them. Detected by a solid state detector and analyzer, these X-rays produces an energy spectrum from which the composition of the irradiated volume can be deduced. Quantitative EDX analysis is only possible for elements with atomic number larger than 10 and with a relative accuracy of about 5 to 15%. The results for light elements are only qualitative.

2.8 Inductively-coupled-plasma-Optical Emission Spectrometer (ICP-OES)

Inductively-coupled-plasma-Optical Emission Spectrometer a high sensitivity instrument used for analyzing metallic elements in solution. Most of the elements can be detected in ppm and some of the elements in ppb level as well.

In emission spectroscopy, thermal energy in the form of plasma is used to excite free atoms as well as in some cases ions to higher energy levels. The atoms or ions will subsequently emit the characteristic radiation that can be isolated by monochromator and detected by the detector (photomultiplier tube), see Fig.2.8. The intensity of emitted radiation is proportional to the concentration of atoms or ions present in the sample. ICP instruments comprise various optical spectrometers, nebulizers (including glass concentric, parallel flow, JY pneumatic, cross flow, V groove, micro concentric, ultrasonic, CMA), spray chambers, ICP torch, and RF generators.

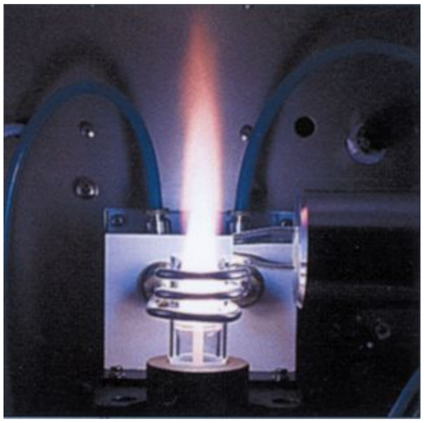

Fig. 2.7 Inductively Coupled Plasma-Optical Emission Spectrometer

Our Co-doped TiO_2 samples were measured in the Chemistry Department of National University of Singapore, Elemental Analysis Laboratory. The equipment is Thermal Jarrell Ash Duo Iris Inductively Coupled Plasma-Optical Emission Spectrometer.

2.9 X-ray Photoelectron Spectroscopy (XPS)

The X-ray photoemission spectroscopy (XPS) is utilized to obtain information on elements and on their chemical bonds, allowing the identification of the different chemical compounds that is possible to find on the surfaces. For example the XPS spectroscopy is easily able to distinguish if floride is in ionic or covalent state, or, for many metallic elements, if they are oxidized or reduced. This technique gives information on the first atomic layers, although it is possible to study the deeper layers by using the ionic sputtering too. The atomic sensitivity is about 0.1% and it is able to detect all the elements unless H and He. XPS can be used to study all solid samples, including insulators like glasses and polymers.

2.9.1 Principle of XPS

XPS is an analytical technique based on the photoelectric effect. When x-ray strike the sample, a core electron can absorb the energy and be emitted. This electron is called a photoelectron. This step is called excitation, because the atom loses an electron and is in an excited state. After the photoelectron is emitted, an electron from an outer shell can drop to fill the vacant site created. This is called relaxation. To maintain the energy balance, a photon can be emitted, or an Auger electron can be expelled from outer shells. In the XPS technique, the energies of the photoemitted electrons are measured, and information on the types of elements present and their chemical state are obtained.

2.9.2 Qualitative analysis

The kinetic energies (and thus the binding energies) of the photoemitted electrons are obtained. Fig.2.8 shows a typical XPS spectrum. Each peak can be related to a certain core level, since these energies are characteristic of each level. In a typical analysis, a broad survey scan is conducted over a wide energy range. Some portions of the spectrum often must be analyzed over a narrower energy range to obtain details. Comparison with spectra from pure elements is very helpful when performing qualitative analysis.

Changes in the chemical environment cause shifts in the binding energy of core electrons, and one of the most important capabilities of XPS is to measure these shifts. The changes in the binding energy are called chemical shifts and can result from a change in the nearest neighbor, the oxidation state, the compound, or the crystal structure.

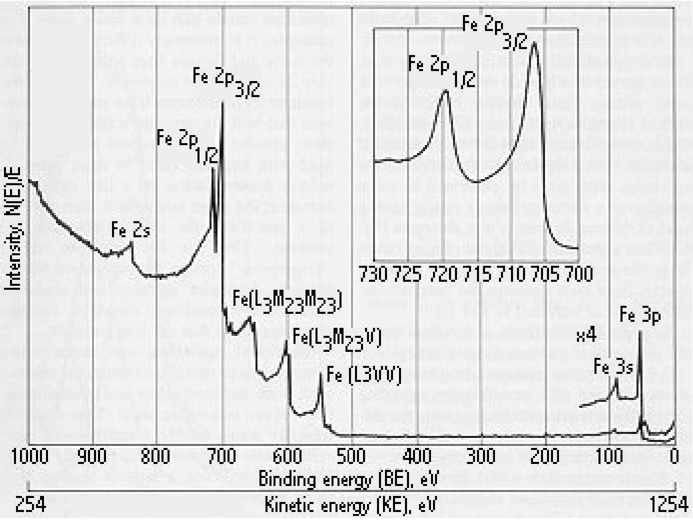

Fig.2.8 XPS spectrum of iron

Reference:

[1] R. Behrisch, "*Sputtering by particle bombardment*", Berlin; New York: Springer-Verlag, 1981-c1991

[2] W.D. Westwood, "*Sputtering Deposition*", Best of industry-short course series notes

[3] G. Knuyt, C. Quaeyhaegens, J.D'Haen and L.M. Stals, *Thin Solid Films*, **258,** 159 (1995)

[4] S. Foner, "Versatile and sensitive vibrating sample magnetometer", *Rev. Sci. Inst.* **30,** 548 (1959)

[5] S.L. Flegler, J.W. Heckman, and K.L. Klomparens, "*Scanning and transmission electron microscopy: an introduction,*" New York: W.H. Freeman, (1993)

[6] John L. Vossen, Werner Kern, "*Thin Film Processes*", p106, New York: Academic Press, (1978)

[7] John L. Vossen, Werner Kern, "*Thin Film Processes*", p158, New York: Academic Press, (1978)

[8] Editors: David A. Glocker, S. Ismat Shat, "Handbook of Thin Film Process Technology", Bristol, UK; Philadelphia: Institute of Physics Pub., (1995)

[9] http://srdata.nist.gov/xps/index.htm

Chapter 3 CoZr System

In this chapter, CoZr system is investigated for the application of phase transition method for nanopatterning. The magnetic properties and microstructures are discussed in detail.

3.1 Literature Review

In the formal chapter, we introduce one approach of magnetic nanopatterning via nanoscale magnetic phase change. Suitable materials for magnetic phase change are those with shorter phase change time and lower phase change temperature.

CoZr system could be a candidate for this method because it can change from non-magnetic to magnetic state by annealing. A few works have been reported on rapidly quenched CoZr bulk alloys [2-9]. In these reports, two ferromagnetic compounds were revealed. One of them was originally reported [1] as $Co_{11}Zr_2$ (=15.4% Zr). The other is cubic $Co_{23}Zr_6$ phase (=20.7 at% Zr).

The $Co_{11}Zr_2$ phase has a Curie temperature T_c at about 500 ºC [3,5,7-9] and is believed to be responsible for the magnetic hardness in the rapidly quenched alloys. Its magnetocrystalline anisotropy was estimated to be uniaxial with an anisotropy field of about 35 K Oe [5,7,9]. Up to date, the crystal structure of the $Co_{11}Zr_2$ phase remains uncertain. Among the investigations, most groups believe $Co_{11}Zr_2$ has two kinds of possible structures. One is orthorhombic with two long-period superlattices in antiphase relation to one another along [100] direction [8]. The other proposed structure of $Co_{11}Zr_2$ has a pseudohexagonal symmetry [10]. In the ref. [10], it is believed that the structure of $Co_{11}Zr_2$ is related to Ni_5Zr. The cubic cell of Ni_5Zr, when it is stood up on the cube diagonal, can be reinterpreted as a hexagonal cell ($a_{hex}=a_{cub}/\sqrt{2}$, $c_{hex}=a_{hex}\sqrt{3}$). Moreover, the Ni_5Zr structure itself consists of rampled layers of the $CaCu_5$ type stacked in a sequence, A, B, C…. The related $Co_{11}Zr_2$ phase, then, mimics the Co-rare-earth metal (RE) compounds in structure, the principle difference being that, whereas RE atoms share a common plane with Co atoms, the Zr atoms (that have a smaller atomic radius) tend to move out of this plane somewhat. For this reason, the unit cell of CoZr has shorter *a* axis and longer *c* axis, which lead to pseudohexagonal symmetry.

The $Co_{23}Zr_6$ phase has a cubic structure and is magnetically soft. Thermomagnetic analysis revealed that the Curie Temperature is 180°C [5,9,10].

Two magnetic compounds were mostly investigated by rapidly quenched method. The Co-Zr alloy ingots were prepared by arc-melting in an argon atmosphere. After that, these ingots were homogenized at 1423 K for 20 h and quenched in water [10]. This rapidly quenched method has complicated procedures, which is not suitable for low-cost and large-scale application.

Little work has been carried out on CoZr thin films so far. However, due to the dimension effect, CoZr thin film may be significantly different from bulk one. It is a promising candidate to obtain the phase transition from non-magnetic state to magnetic state through the formation of magnetic phases, especially the hard magnetic phase $Co_{11}Zr_2$. In this work, we modified the parameters of sputtering method to find the non-magnetic area of CoZr thin films. Further, post-annealing treatment was investigated in detail, which may induce the phase change in the films. Characterization focused on the microstructure and magnetic properties of CoZr films, which have different deposition and post-annealing parameters.

3.2 Experiments

A series of $Co_{1-x}Zr_x$ thin films were deposited on the glass substrate directly at room temperature. Magnetron co-sputtering method was used with Co and Zr metallic targets. Zr atom concentration in them is from 0 at% to 70 at%, and the thickness of the films is about 50 nm. During the sputtering, the base pressure and the work pressure were 5×10^{-7} Torr and 5 mTorr, respectively (working gas is Argon). Different Zr concentrations are obtained by changing power densities of Co and Zr targets in order to change their sputtering rate ratio.

Table 3.1 $Co_{1-x}Zr_x$ thin films deposition parameters

sample	Zr at%	P(base) (1E-7 Torr)	P(Ar) (mTorr)	Power(Co) (W)	Power(Zr) (W)	co-sputtering time (s)
CoZr020529C	0%	6.9	5	50	0	384
CoZr020404E	10%	4.6	5	50	14	519
CoZr020404F	15%	6.0	5	50	21	463
CoZr020401E	20%	7.0	5	50	30	412
CoZr020520A	30%	6.0	5	50	47	201
CoZr020404A	40%	6.7	5	50	72	264
CoZr020404B	50%	6.3	5	30	66	334
CoZr020404C	60%	6.0	5	30	98	249
CoZr020404D	70%	4.0	5	15	80	336

As-deposited samples were annealed at different temperature (400°C-600°C) and different time (2-13 hours) in vacuum furnace with the base pressure of 5×10^{-6} Torr.

Magnetic properties were studied by a vibrating sample magnetometer (VSM). Curie temperatures of the magnetic phases were measured using the thermomagnetic analysis (TMA) with magnetic field of 1000 Oe. Crystal structure and phase analysis were done by x-ray diffraction (XRD) and transmission electron microscopy (TEM). Energy dispersive x-ray analysis (EDX) was used for elemental analysis.

3.3 Results and Discussion

3.3.1 Zr content dependant property

3.3.1.1 As-deposited state

In as-deposited state, with the increasing of Zr concentration, $Co_{1-x}Zr_x$ films change gradually from soft magnetic state (x<60 at%) to non-magnetic state (x>60 at%) (Fig.3.1). XRD results show that all the as-deposited samples appear to be amorphous.

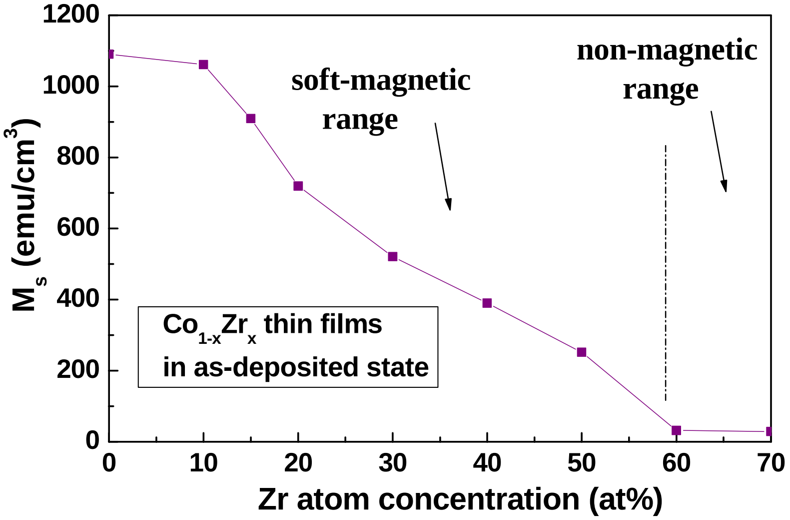

Fig.3.1 Saturation magnetization of $Co_{1-x}Zr_x$ thin films in as-deposited state

3.3.1.2 Post-annealed state

With post-annealing treatment, the magnetic properties are enhanced in all annealed samples (Zr at% from 10% to 70%). Fig.3.2 shows the Zr concentration dependence of saturation magnetization (M_s) for as-deposited and annealed samples. The annealing temperatures were 400°C, 500°C, 600°C, respectively. Annealing time was fixed at 2 hours. The diagram clearly shows that the enhancement of magnetic properties was achieved in all annealed samples. Saturation magnetization increases following the annealing temperature.

Especially, there is a dramatic increase in M_s for $Co_{40}Zr_{60}$ films by annealing (inset of Fig.3.2). In as-deposited state, $Co_{40}Zr_{60}$ is non-magnetic. After post-annealing treatment, a sharp increase of M_s begins at 500°C and the value of M_s reaches 231 emu/cm^3 after annealing at 600°C. This kind of obvious transition from non-magnetic to magnetic state is very important and useful for the candidate, which is to make patterned media through phase transition method. In the following section 3.3.2, we focus on the property investigations of this set of samples, which have 60% Zr concentration.

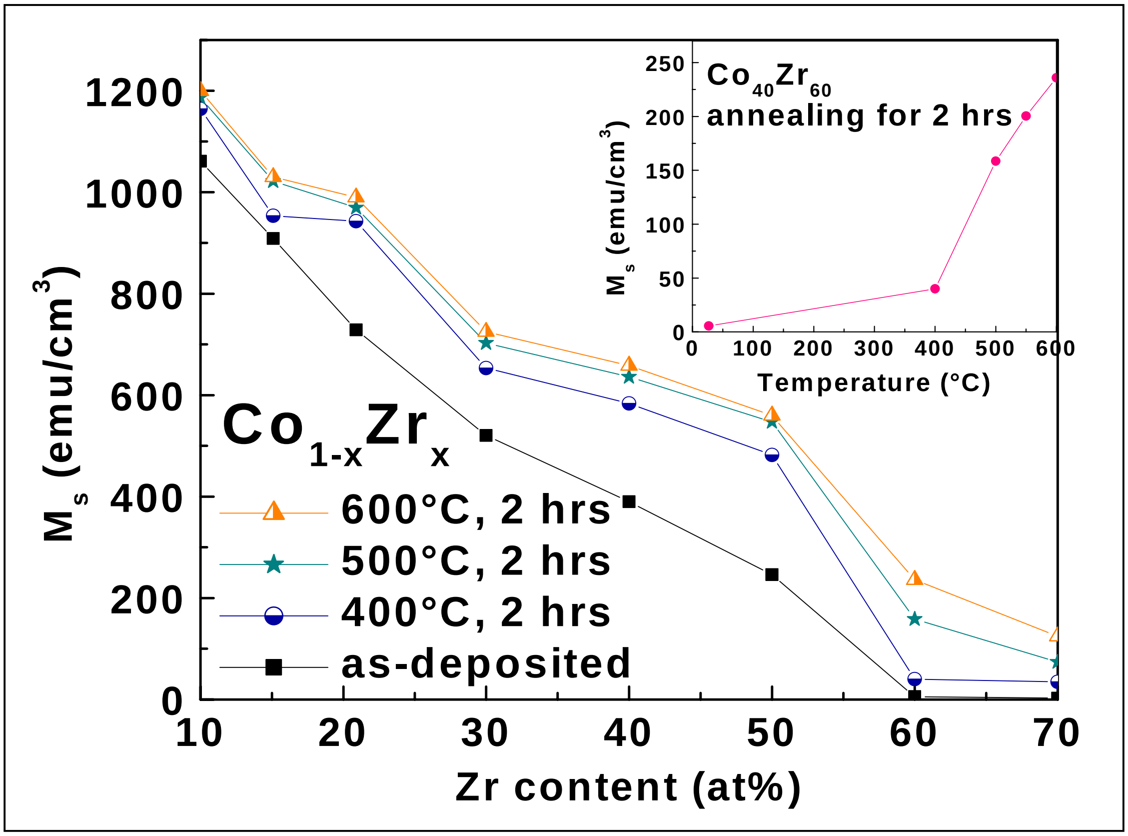

Fig. 3.2: Saturation magnetization (M_s) as a function of the Zr concentration at different annealing temperatures (annealing time is 2 hours). Inset shows temperature dependence of M_s of $Co_{40}Zr_{60}$ films after annealing for 2 hours.

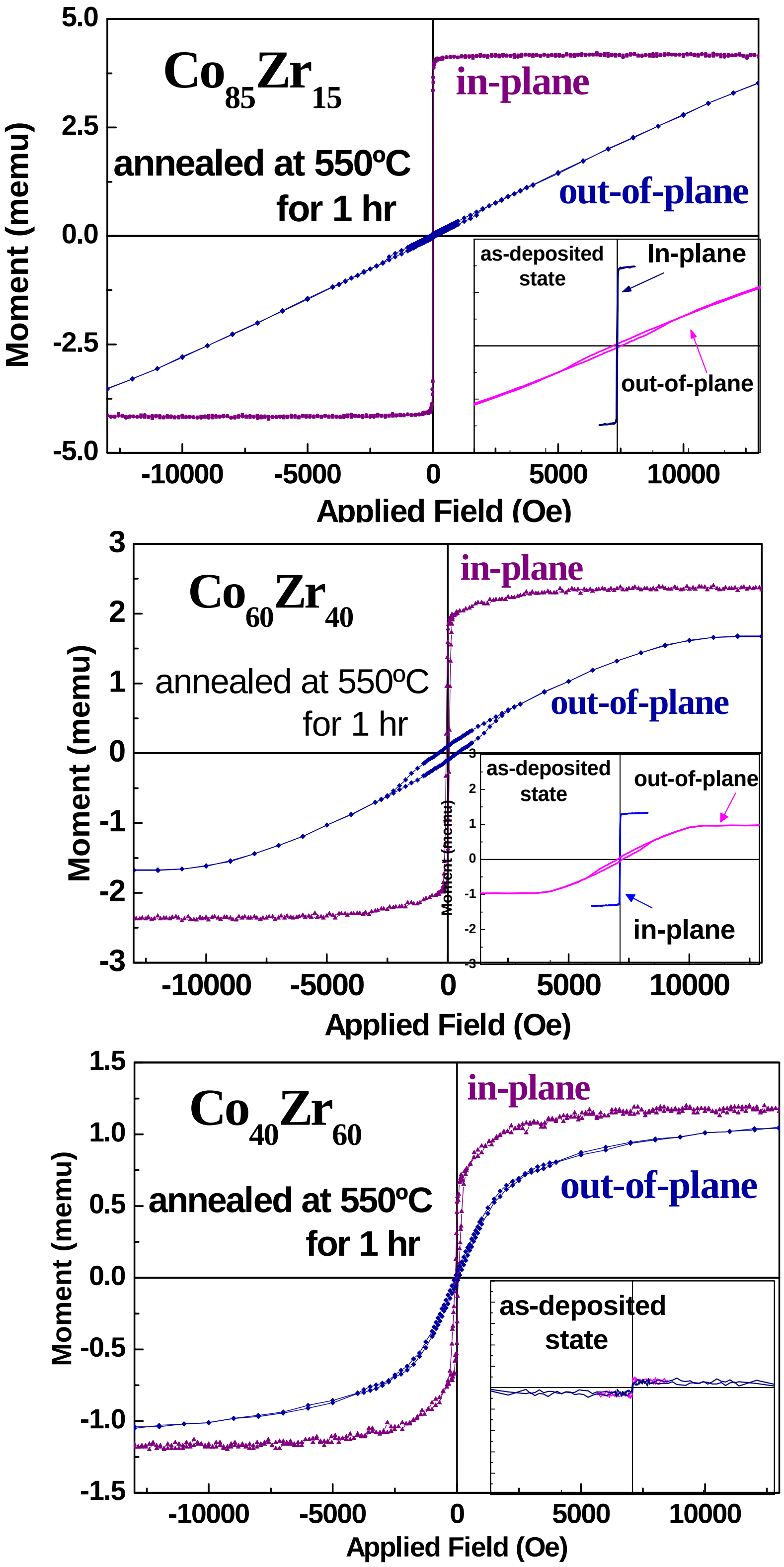

Fig.3.3 the development of in-plane and out-of-plane hysteresis loops of annealed $Co_{1-x}Zr_x$ films following the change of Co concentration.

In annealed samples, we also find out that the samples with different Zr concentration have different magnetic properties, even with the same annealing conditions. Fig.3.3 shows the development of in-plane and out-of-plane hysteresis loops of annealed $Co_{1-x}Zr_x$ films following the change of Co concentration. In $Co_{85}Zr_{15}$ film, the in-plane hysteresis loop has very high squareness, while the out-of-plane loop is almost linear. This behavior is much like that of Stoner-Wohlfarth particles, which have coherent rotation. It also shows the film has strong anisotropy with the easy axis lying in the plane. With the decrease of Co concentration, the annealed films change from anisotropic to almost isotropic.

3.3.2 Detailed studies on $Co_{40}Zr_{60}$ thin film samples

In as-deposited state, $Co_{40}Zr_{60}$ samples are non-magnetic with amorphous structure. Post-annealing effect was studied in two ways. One is changing annealing temperature (400°C, 500°C, 600°C), when fixing annealing time at 2 hours. The other way is changing annealing time (2, 5, 8 hours), when fixing annealing temperature at 550°C.

3.3.2.1 Phase studies

The x-ray diffraction patterns of this set of samples are shown in Fig.3.4. An obvious change in the crystal structure appears when annealing temperature is above 550°C. It is interesting to notice that the annealing temperature needed for phase change is much lower in CoZr thin films than that in rapidly quenched CoZr bulk samples [3-6]. The XRD of these annealed samples contains $Co_{23}Zr_6$ (400) and (620) peaks and three peaks of $Co_{11}Zr_2$ phase. It shows that hard magnetic phase $Co_{11}Zr_2$ and ferromagnetic phase

$Co_{23}Zr_6$ are formed in annealed $Co_{40}Zr_{60}$ films. Up to date, the crystal structure of $Co_{11}Zr_2$ phase remains uncertain. A few standard references show the positions of the XRD peaks of $Co_{11}Zr_2$ phase, but none of them point out the corresponding crystal orientations. The structure of $Co_{11}Zr_2$ is believed to closely relate to that of cubic Co_5Zr. One can see that the cubic cell of FCC Co_5Zr can be reinterpreted as hexagonal cell when it is stood up on the cube diagonal ($a_{hex}=a_{cub}/\sqrt{2}$, $c_{hex}=a_{cub}\sqrt{3}$) [6]. In the case of $Co_{11}Zr_2$, which has a slight more Co atoms than Co_5Zr, it will tend to approach the pseudohexagonal or orthorhombic cell from above hexagonal cell ($a_{orth}=a_{hex}$, $b_{orth}=a_{hex}\sqrt{3}$, $c_{orth}=c_{hex}$). In our experiments, it is also difficult to index the three peaks of $Co_{11}Zr_2$ phase. But we find that peak positions of both phases shift to low angle. It may due to the enlarged lattice spacing affected by extra Zr atoms in $Co_{40}Zr_{60}$ films. Except for the existence of these two binary compounds, XRD patterns indicate no sign of Co or Zr crystal phases in annealed samples. This suggests that Co may be in the state of binary compounds and extra Zr are in amorphous state.

Table 3.2 Standard diffraction data of two magnetic phases

Phase	Crystal plane	Standard 2θ value	Intensity in the standard data sheet
$Co_{23}Zr_6$	(400)	44.369°	100
	(620)	50.107°	10
$Co_{11}Zr_2$	unclear	51.345°	50
	unclear	60.067°	20
	unclear	82.425°	100

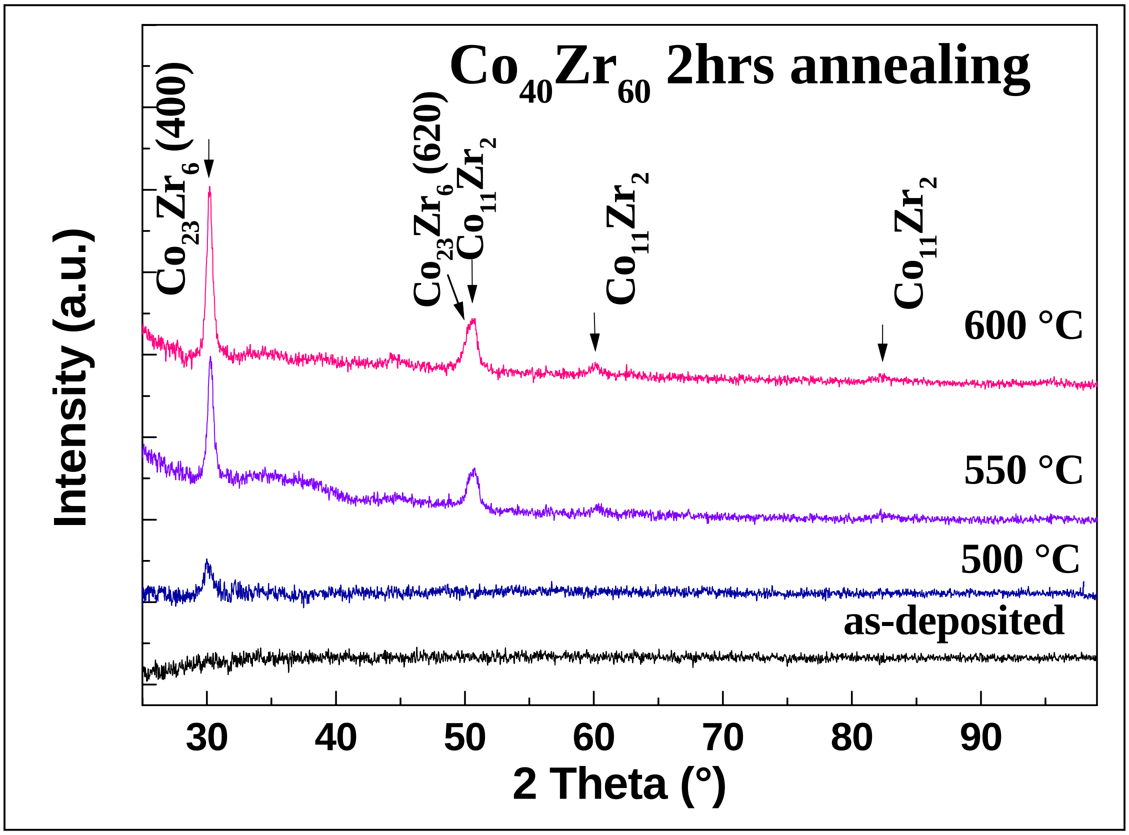

Fig.3.4 XRD patterns of $Co_{40}Zr_{60}$ as-deposited sample and annealed samples.

Through the characterization of XRD (Fig.3.4), two magnetic phases are found in annealed samples. They are soft magnetic $Co_{23}Zr_6$ and hard magnetic $Co_{11}Zr_2$. Pure $Co_{11}Zr_2$ sample has much largerer H_c than that of pure $Co_{23}Zr_6$ sample. But our annealed samples show a rather continuous switching with a single H_c based on their hysteresis loops (Fig.3.3 in section 3.3.1.2). This phenomenon may due to the exchange coupling between the soft and hard magnetic phases. Many publications have reported on this kind of exchange coupling [11, 12, 13]. Some of them investigate soft/hard magnetic interlayer coupling. In the interface, there exists a strong magnetic interaction between soft and hard magnetic layers, which make their magnetization switch together. In our samples, the two phases are formed during annealing process. It will make them distribute randomly and mix together in a high degree. Thus strong interaction between these two magnetic phases may exist, which result in the synchronic switching in the hysteresis loops.

3.3.2.2 Thermomagetic analysis (TMA) and related calculation

To further confirm the existence of these two magnetic compounds, thermomagnetic analysis (TMA) has been studied on annealed $Co_{40}Zr_{60}$ samples. Thermomagnetic analysis was done by the vibrating sample magnetometer. During the measurements, the sample temperature was changed from 300 K to 1000 K, and applied field is fixed at 1000 Oe. Two obvious drops of M_s appeared at about 450 K and 780 K (Fig.3.5), which are quite close to the Curie temperatures of $Co_{23}Zr_6$ and $Co_{11}Zr_2$, respectively [3,5,6].

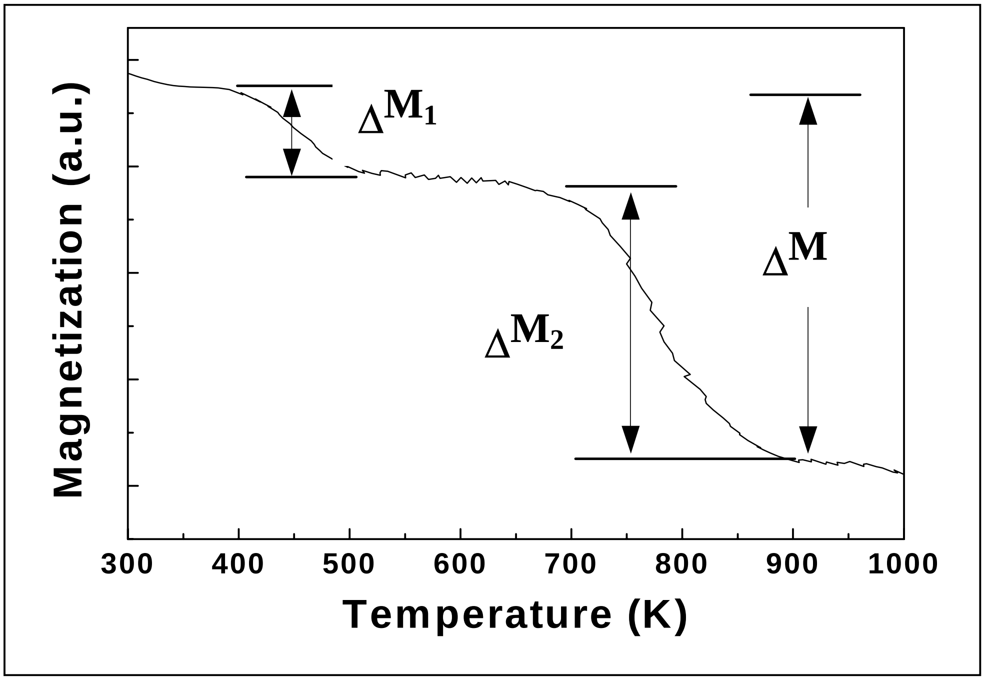

Fig. 3.5: TMA curve of annealed $Co_{40}Zr_{60}$ sample (550 °C, 2 hours). ΔM is the total reduction of the magnetization during TMA. ΔM1 and ΔM2 are magnetization changes at around two Curie temperatures.

Based on XRD results, there are only two magnetic phases in post-annealed samples, $Co_{11}Zr_2$ and $Co_{23}Zr_6$, and Zr is in the amorphous state. Thus, when the temperature increases, the decreases of the magnetization at temperatures of 450 K and 780 K are determined by the M_s and the volume fraction of the corresponding phases. Based on above analysis, simple calculations of M_s and volume fraction of $Co_{11}Zr_2$ and $Co_{23}Zr_6$ were done based on the experimental data of TMA.

$$M_s = M_{s1}v_1 + M_{s2}(1-v_1) \qquad \text{(eq.3.1)}$$

$$M_{s1}v_1 B = M_{s2}(1-v_1)A \qquad \text{(eq.3.2)}$$

$$M_s^{'} = M_{s1}v_1^{'} + M_{s2}^{'}(1-v_1^{'}) \qquad \text{(eq.3.3)}$$

$$M_{s1}v_1^{'}B^{'} = M_{s2}(1-v_1^{'})A^{'} \qquad \text{(eq.3.4)}$$

The M_s of an annealed sample is consisted of the contributions of $Co_{23}Zr_6$ and $Co_{11}Zr_2$ (eq.3.1). Where, M_{s1} and M_{s2} represent the saturation magnetization per unit volume of $Co_{23}Zr_6$ and $Co_{11}Zr_2$ phases at room temperature. v_1 and $(1-v_1)$ are the volume fractions of $Co_{23}Zr_6$ phase and $Co_{11}Zr_2$ phase, respectively. With the assistance of TMA data, the volume magnetization ($M_{s1}v_1$ or $M_{s2}v_2$) of each magnetic phase can be used to express the total magnetization reduction in the sample individually, when considering the percentage of magnetization reduction (A and B) at around each Curie temperature (eq.3.2). A and B are obtained from each TMA curve (Fig.3.5), ($A = \frac{\Delta M_1}{\Delta M}$, $B = \frac{\Delta M_2}{\Delta M}$). Equations (3.3) and (3.4) are for the second sample. Two selected samples are required to have different volume ratios of $Co_{11}Zr_2$ and

$Co_{23}Zr_6$, as ensures the four equations are independent. So, two annealed $Co_{40}Zr_{60}$ samples with different annealing conditions were chosen. One was annealed at 600°C for 2 hours and the other was annealed 550°C for 5 hours. By solving above four equations with experimental data, the M_s of $Co_{23}Zr_6$ and $Co_{11}Zr_2$ were obtained to be 1066 emu/cm^3 and 924 emu/cm^3, respectively. The volume fractions of $Co_{11}Zr_2$ are 73.2% and 78.9% in the first and second samples, respectively.

In the aspect of derivation, the equations are strict. When two sets of data are from samples with different $C_{23}Zr_6/Co_{11}Zr_2$ ratio, equation (3.1) to (3.4) are independent so that the four variable M_{s1}, M_{s2}, v_1, v'_1 can be derived. During the calculation, the error may come from the instrumental limitations, which may effect the accurateness of six constants in the equations: M_s, M_s', A, A', B, B'. The VSM has high sensitivity on the magnetization measurement, which can limit the experimental error in a small range. Thus this calculation method may not induce large errors.

3.3.2.3 Microstructure studies

Microstructures of annealed $Co_{40}Zr_{60}$ samples were studied by XRD and TEM. The grain sizes of annealed samples were calculated using the Scherrer equation. Considering the polycrystalline property of the films and the distribution of input X-ray, the Scherrer equation is:

$$\beta(2\theta) = \frac{0.90\lambda}{L\cos\theta} \qquad \text{(eq.3.5) [7]}$$

where, mean grain size (L) is inversely proportional to peak breadth at half maximum (FWHM) (β) and $\cos\theta$ (2θ refer to the peak position).

Table 3.3 Calculation of grain sizes of annealed samples with different annealing temperature

annealing temperature (°C)	$\theta_{1/2}$ (degree)	$\beta(2\theta)$	$\cos\theta$	$\beta\cos\theta$	$L = \frac{0.90\lambda}{\beta\cos\theta}$ (nm)
500	0.50	0.008727	0.9654	0.008425	16.5
550	0.60	0.010470	0.9654	0.010108	13.7
600	0.75	0.013090	0.9654	0.012637	11

Thus, the grain sizes of annealed samples are 11.0 nm, 13.7 nm and 16.5 nm, corresponding to annealing temperatures of 500°C, 550°C and 600°C with fixed time of 2 hours (see table 3.2). The grain size increases with annealing temperature, which may also be a source to enhance the magnetic properties of the annealed films.

TEM analyses of the annealed $Co_{40}Zr_{60}$ samples are consistent with XRD results. Fig.3.6 shows one of the selected-area diffraction (SAD) patterns. Based on the SAD patterns, the lattice spacing derived from each ring according to the formula:

$$d = \frac{\lambda C}{R} \qquad \text{(eq.3.6)}$$

Where R is the diameter of each diffraction ring, λ is the wavelength of electron beam, C is the constant parameter of TEM equipment, and *d* is the corresponding lattice spacing.

Table 3.4 Comparison between TEM-SAD results and XRD results

diameter of each SAD ring R (mm)	wavelength of electron beam λ (Å)	constant parameter C (m)	corresponding lattice spacing d (Å)	lattice spacing calculated from XRD d' (Å)
7.0	0.025	0.8	2.857	2.938
11.5	0.025	0.8	1.739	1.788
13.5	0.025	0.8	1.481	1.483
17.5	0.025	0.8	1.143	1.166
20.0	0.025	0.8	1.000	1.030

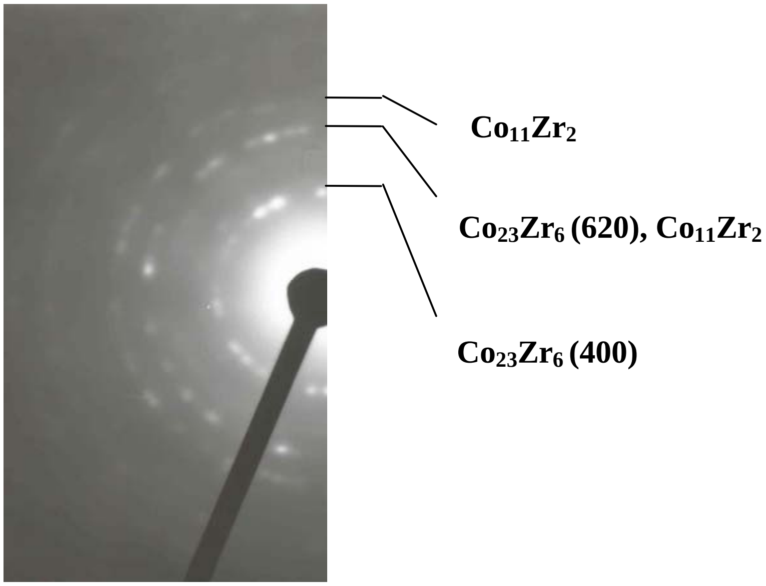

Fig. 3.6 : SAD pattern of annealed $Co_{40}Zr_{60}$ sample (550°C, 13 hours).

$Co_{11}Zr_2$ and $Co_{23}Zr_6$ phases were formed.

From table 3.3, it is proved that the SAD patterns agree well with XRD results. As one can see in Fig.3.6, these diffraction rings are not continuous, but are consisted of many diffraction dots. It may indicate that the annealed film has polycrystalline structure, but grains have orientations. EDX results combining with SAD analysis reveal that the crystal phases are Co-rich among Zr-rich matrix.

3.3.2.4 Annealing time effect studies

Annealing time effect was also studied by changing annealing time from 2 hours to 13 hours at temperature of 550°C. XRD patterns are similar as those of the different annealing temperature series, which had two crystal phases $Co_{23}Zr_6$ and $Co_{11}Zr_2$. M_s increases with annealing time and reaches 261 emu/cm^3 after 13 hours annealing (see Fig.3.7).

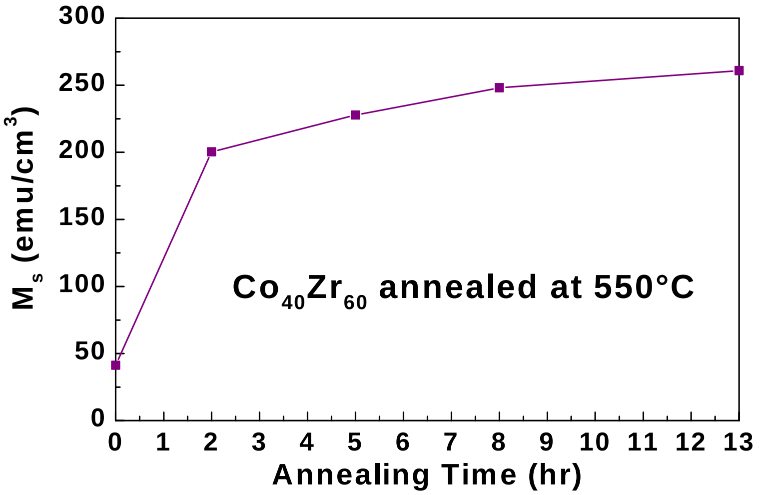

Fig.3.7 Saturation Magnetization (M_s) dependent on annealing time of $Co_{40}Zr_{60}$ samples (fixed annealing temperature at 550 °C).

All annealed samples show a perpendicular magnetic anisotropy (see Fig.3.8). The out-of-plane coercivity of this series samples increases first with annealing time, and then decreases. The maximum value appears after around 5 to 8 hours annealing. The formation of magnetic phases $Co_{11}Zr_2$ and $Co_{23}Zr_6$ is the main reason for the enhancement of H_c (both in-plane and out-of-plane directions). While, when the annealing time is too long (13 hrs), the H_c decreases. The possible reason may be the oxidation of CoZr films. During the annealing, the vacuum is at about $5*10^{-6}$ Torr. With long annealing time at 550°C, the film may interactive with oxygen in the surface area.

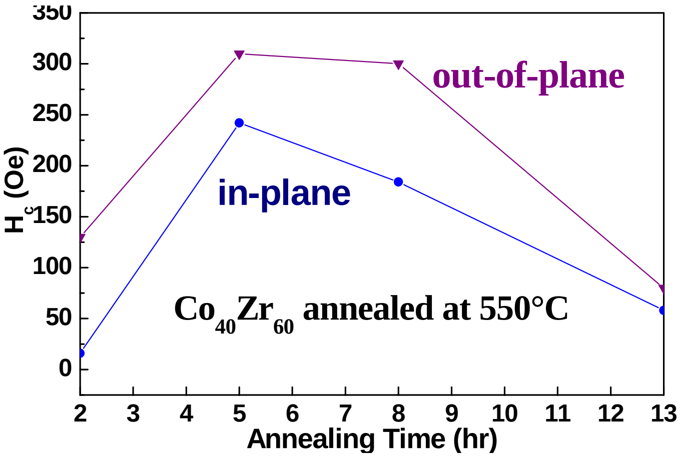

Fig.3.8 Out-of-plane coercivity dependent on annealing time of $Co_{40}Zr_{60}$ annealed samples (fixed annealing temperature at 550°C)

3.4 Summary

$Co_{1-x}Zr_x$ sputtered thin films have been investigated in this work. In as-deposited state, with the increasing of Zr concentration, $Co_{1-x}Zr_x$ films change gradually from soft magnetic state (x<60 at%) to non-magnetic state (x>60 at%). Post-annealing treatment can effectively improve the M_s of CoZr films. The M_s of annealed samples increases with the annealing temperature. Especially, there is a dramatic increase in M_s for $Co_{40}Zr_{60}$ films after annealing.

Detailed work has been done on $Co_{40}Zr_{60}$ films. Phase change from non-magnetic state to magnetic state occurs in $Co_{40}Zr_{60}$ thin films when annealing at 550°C for 2 hours. The annealing temperature needed for phase change is much lower than that of rapidly quenched samples. $Co_{11}Zr_2$ and $Co_{23}Zr_6$ magnetic phases are formed after annealing, which lead to the enhancement of the magnetism of annealed samples. And, the calculations on TEM-SAD patterns show that the enlarged grain size may be another source. Moreover, M_s of these two phases were calculated based on TMA data. Perpendicular magnetic anisotropy is revealed in annealed samples. The out-of-plane coercivity of this series samples has the maximum value after around 5 ~ 8 hours annealing.

Reference:

[1] W.H. Pechin, D.E. Williams, W.L. *Larsen, Trans*. ASM **57**, 464 (1964)

[2] A.M. Ghemawat, M. Foldeaki, R.A. Dunlap, R.C. O'Handley, *IEEE Trans. Magn*. **25**, 3312 (1989)

[3] C. Gao, H. Wan, G.C. Hadjipanayis, *J. Appl. Phys*. **67**, 4960 (1990)

[4] G. Stroink, Z.M. Stadnik, G. Viau, R.A. Dunlap, *J. Appl. Phys*. **67**, 4963 (1990)

[5] T. Ishikawa, K. Ohmori, *IEEE Trans. Magn*. **26** 1370 (1990).

[6] B.G. Shen, H.Q. Guo, L.Y. Yang, J.X. Zhang, J.G. Zhao, *Phys. Status Solidi A* **121**, K105 (1990)

[7] E. Burzo, R. Grossinger, P. Hundegger, H.R. Kirchmayr, et al. *J. Appl. Phys*. **70**, 6550 (1991)

[8] S.F. Cheng, B.G. Demczyk, W.E. Wallace, Proceedings of the Sixth International Symposium on Magnetic Anisotropy and Coercivity in Rare Earth-Transition Metal Alloys, Pittsburgh, PA, p.477 (1990).

[9] A.M. Gabay, Y. Zhang, G.C. Hadjipanayis, *J. Magn. Magn. Mater*. **236**, 37 (2001)

[10] H.H. Stadelmaier, T.S. Jang, E.-Th. Henig, *Mater. Lett.* **12**, 295 (1991)

[11] G. Gubbiotti, G. Carlotti, M. Madami, et al. *IEEE Trans. Magn*. **38**, 2779 (2002)

[12] E. Goto, N. Hayashi, T. Miyashita, and K. Nakagawa, *J. Appl. Phys.*, **36**, 2951 (1965)

[13] E.E. Fullerton, J.S.Jiang, M. Grimsditch, et al. *Phys. Rev. B*, **58**, 12193 (1998)

Chapter 4 Co-doped TiO_2 System

This chapter focuses on the research work of Co-doped TiO_2 *system based on the results of ICP, XPS, TEM, and AGM. Different layer structures of samples are investigated. The binding state and neighbor environment of Co and Ti, the microstructure and magnetic property of samples are discussed in detail.*

4.1 Literature Review

Since its initial discovery nearly 2 years ago, Co-doped TiO_2 has attracted considerable interest, and controversy, because it exhibits ferromagnetism at and above room temperature. This material has potential as a magnetically robust diluted magnetic semiconductor (DMS) that may be useful as a room-temperature spin injector for semicondutor heterostructures. TiO_2 has three kinds of crystal structure, rutile, anatase, and brookite, composed of Ti ions having octahedral coordination. They are wide gap oxide semiconductors, and rutile is the most thermal stable phase. Co-doped anatase may also find application in spin optoelectronics due to the fact that it is optically transparent. That this material is an n-type semiconductor makes it attractive for spintronics because electrons exhibit considerably longer spin relaxation times than holes in most semiconductors [4].

The nature of the controversy over this material has to do with the extraordinarily high value of the Curie temperature (T_c), which is well above room temperature. It is unanticipated and unprecedented that electron mediated exchange interaction would generate such a strong ferromagnetic interaction. While the mechanism of magnetism has not yet been definitively elucidated, there are indicators that this material may be a true itinerant-electron DMS. By now, $Co_xTi_{1-x}O_{2-x}$ has been grown by pulsed laser deposition [3,6,7], oxygen plasma assisted molecular beam epitaxy (OPA-MBE) [2,4,5], Sputtering [7,8], Chemical Vapor Deposition [15], and Sol-gel processing [13,14]. All the groups reported the ferromagnetic behavior of Co-TiO_2 at room-temperature, and epitaxial films have exhibited T_c values well above room temperature [3-16] .

This result has prompted speculation that the magnetism may be due to Co clusters that form within the material. Indeed, Co clusters have been detected by transmission electron microscopy (TEM) in PLD-grown material in which the background oxygen pressure in the growth chamber was below a certain value [10]. The magnetic hysteresis loops for films with Co nanoclusters yielded a saturation moment of 1.7 u_B per Co, the value of Co metal. However, the same study showed the extent of Co metal cluster formation decreased as the oxygen background pressure increased, suggesting more complete Co dispersion and incorporation within the anatase lattice. Moreover, the saturation moment was reduced to 0.3 $\mathrm{u_B}$ per Co upon dispersion, the same value originally measured by Matsumoto et al. [3,6]

In contrast, OPA-MBE grown epitaxial Co-doped anatase does not contain any elemental Co. Co K-shell near-edge and extended x-ray absorption fine structure results clearly show that all Co is Co (II), and that Co substitutes for Ti in the lattice [2]. The saturation moment in OPA-MBE grown films ranges from 1.1 to 1.3 u_B per Co, which is close to the value expected for low-spin Co in a DMS [2,15,16].

4.2 Experiments

4.2.1 Thin film deposition

Co-doped TiO_2 thin films were deposited by magnetron sputtering method at room-temperature. $LaAlO_3(001)$ and $SrTiO_3(001)$ single crystals were used as substrates. The lattice mismatch between $TiO_2(001)$ and $LaAlO_3(001)$ is –0.26%, and it is –3.1% between $TiO_2(001)$ and $SrTiO_3(001)$ [1,2]. We focus our research on the low mismatch series ($LaAlO_3$).

In order to investigate the behavior of Co atoms in TiO_2 matrix, two kinds of layer structures were designed for $Co_xTi_{1-x}O_2$ thin films (Fig.4.1). One is pure multilayer structure: substrate/$(TiO_2/Co)_n/TiO_2$, the other is partial co-sputtering structure: substrate/$(TiO_2/Co_xTi_{1-x}O_2)_n/TiO_2$. The difference in the structures is the different number of repeated layers between the substrate and cap layer (TiO_2). And the number of each pair of repeated layers is represented by n, which is used to control the Co concentration in the films. We fixed the thickness of each Co layer (4 Å) and $Co_xTi_{1-x}O_2$ layer (5.15 Å). And the number of inserted layers (Co or $Co_xTi_{1-x}O_2$) is 1,3,5,7, corresponding to different Co concentration. The total thickness of samples was fixed at 100 nm. Table 4.1 introduces the detailed parameters of the samples prepared.

Metallic Co target and isolated TiO_2 target were used, and were controlled by DC and RF power supply, respectively. The base pressure during sputtering was about 5×10^{-7} Torr and the working pressure of Ar gas was fixed at 2.5 mTorr. The sputtering rate of TiO_2 and Co targets are 0.1616 Å/s and 0.5599 Å/s, respectively, based on the sputtering calibration.

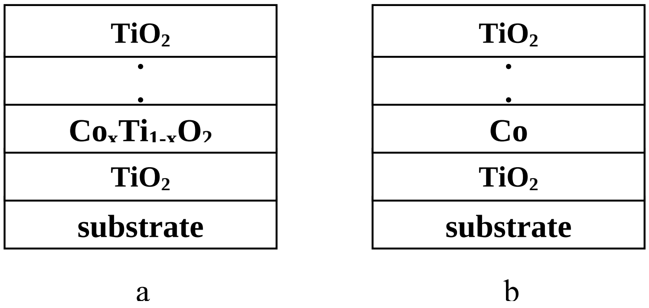

Fig.4.1 Schematic pictures of sample layer structures.
(a) partial co-sputtering structure (b) pure multilayer structure.

Table 4.1 The list of as-deposited samples with different layer structures

sample	substrate	structure	n
		(multilayer)	
CTO031403	LaAiO$_3$	LaAlO3/ $(TiO_2/Co)_1$/ TiO_2	1
CTO031404	LaAiO$_3$	LaAlO3/ $(TiO_2/Co)_3$/ TiO_2	3
CTO031405	LaAiO$_3$	LaAlO3/ $(TiO_2/Co)_5$/ TiO_2	5
CTO031406	LaAiO$_3$	LaAlO3/ $(TiO_2/Co)_7$/ TiO_2	7
		(partial co-sputtering)	
CTO031407	LaAiO$_3$	LaAlO3/ $(TiO_2/CoTiO_2)_1$/ TiO_2	1
CTO031501	LaAiO$_3$	LaAlO3/ $(TiO_2/CoTiO_2)_3$/ TiO_2	3
CTO031502	LaAiO$_3$	LaAlO3/ $(TiO_2/CoTiO_2)_5$/ TiO_2	5
CTO031503	LaAiO$_3$	LaAlO3/ $(TiO_2/CoTiO_2)_7$/ TiO_2	7

Four individual samples were prepared for the characterization of Co concentration, which was done by Inductively-Coupled-Plasma Optical Emission Spectroscopy (ICP-OES). The deposition conditions are the same as above. PMMA substrate was used, and the film structure is PMMA/TiO_2/Co/TiO_2.

4.2.2 Post annealing treatment

For two kinds as-deposited samples with multilayer structure, post annealing treatment is very important to induce the diffusion of Co into TiO_2 layer or TiO_2 matrix. We change the annealing temperature from 400°C to 600°C, when fixing the annealing time at 1 hour. In order to reduce the difference of annealing conditions, all the as-deposited samples with different layer structure and different Co concentration were annealed at the same time under each annealing temperature. Vacuum pressure is about 5×10^{-4} Torr.

4.2.3 Characterization

The important part of research on binding state and neighbor environment of Co and Ti were done by x-ray photoelectron spectroscopy (XPS). Because XPS is surface sensitive, samples were ultrasonically cleaned on the bench using ion-free water before the measurement. All the XPS experiments were done with the help of the FRC group in DSI. Inductively-coupled-plasma optical emission spectrometry (ICP-OES) has high sensitivity on metal mass, and was used to determine Co concentration in the films. The samples prepared for ICP were first dissolved in hot H_2SO_4 (260°C) before the measurement. ICP-OES measurement was done in the elemental analysis laboratory of the Chemistry Department of NUS. Transmission electron microscopy and x-ray diffraction measurement were carried out for the research of phase and microstructure. For the measurement of magnetic properties, alternating gradient force magnetometer and low-temperature vibrating sample magnetometer were used.

4.3 Results and Discussion

4.3.1 Co concentration analysis (ICP result)

According to the previous work of Y. Matsumoto group [3], the solubility limit of Co in anatase TiO_2 is about 8 at%. Therefore, less than 10 at% of Co atom percent was designed in Co-doped TiO_2 samples, and the minimum difference between two samples is about 2 at%. Thus high resolution of characterization method is required to make precise component analysis. Inductively-Coupled-Plasma Optical Emission Spectrometry (ICP-OES) can detect most of the elements up to ppm level, which can meet our requirement.

Table 4.2 ICP-OES results of $Co_xTi_{1-x}O_2$ thin films

sample	results				designed
	Co mass %	Ti mass %	Co/Ti at%	Co at%	Co at%
CTO031604	0.05280	2.11000	0.0203	1.99%	1.34%
CTO031605	0.00849	0.16051	0.0430	4.12%	3.63%
CTO031606	0.01241	0.16925	0.0596	5.62%	6.32%
CTO031607	0.01970	0.15655	0.1023	9.28%	8.92%

Table 4.2 shows the detailed ICP results. Based on the mass ratio of Co and Ti obtained from ICP, we calculated the Co atomic percent in $Co_xTi_{1-x}O_2$ films. The difference between the values that we designed and the ICP results is small, less than 0.7 at%. The

minimum is 0.07 at%, which indicates the precise control of Co concentration in our experiments.

Based on the ICP results, we can also calculate the thickness of each layer in as-deposited state. We assume that the total Co thickness in the film is t nm, so TiO_2 is (100-t) nm. Thus, in as-deposited films, the atomic ratio of Co to Ti (Co/Ti at%) can be expressed by:

$$\frac{Co}{Ti}\ at\% = \frac{\dfrac{thickness(Co) \times \rho(Co)}{M(Co)}}{\dfrac{thickness(TiO_2) \times \rho(TiO_2)}{M(TiO_2)}} \qquad \text{(eq.4.1)}$$

$$= \frac{\dfrac{t \times 8.9}{58.933}}{\dfrac{(100-t) \times 4.2743}{79.8988}} = 2.823 \times \left(\frac{t}{100-t}\right) \qquad \text{(eq.4.2)}$$

Where: $\rho(Co) = 8.9$ (g/cm^3) M(Co)=58.933 (g/mol)

$\rho(TiO_2 - rutile) = 4.2743$ (g/cm^3) M(TiO_2)=79.8988 (g/mol)

Table 4.3 shows the calculation results of each layer thickness in as-deposited samples. In most of the samples, the layer thickness is very close to the value we designed. Only the samples with one Co or $CoTiO_2$ layer have a relatively higher value than expected. It seems that, when n increases, the error of each insert layer will become small. This phenomenon may have the following possible reason. Designed Co layer is 4 Å. With 0.5599 Å/s average growth rate, the deposition should controlled at 7 s. For magnetic sputtering system, the actual start and end of film deposition are controlled by the open and close of the shutter at the top of the target. Thus, there may exist systematic error due to the asynchronous action of the shutter and control button. There may also have few tiny errors, which result in the aberration of the ultra thin layer thickness. Such kind of aberration may be positive or negative, that is, the thickness of the Co layer may be a little larger or smaller than 4 Å. Thus, when the number of the inserted Co layer (n) increases, the error of the average insert layer thickness will decrease.

Table 4.3 Calculation results on each layer thickness in as-deposited samples based on ICP results.

pure multilayer structure				
Co/Ti ratio (ICP result)	total Co thickness (t)	number of layers (n)	each Co layer thickness	designed Co layer thickness
0.0203	0.714 nm	1	0.714 nm	0.4 nm
0.043	1.500 nm	3	0.5 nm	0.4 nm
0.0596	2.068 nm	5	0.41 nm	0.4 nm
0.1023	3.500 nm	7	0.50 nm	0.4 nm
partial co-sputtering structure*				
Co/Ti ratio (ICP result)	total Co thickness (t)	number of layers (n)	Co thickness in each CoTiO2 layer	each CoTiO2 layer thickness
0.0203	0.714 nm	1	0.714 nm	0.920 nm
0.043	1.500 nm	3	0.50 nm	0.644 nm
0.0596	2.068 nm	5	0.41 nm	0.533 nm
0.1023	3.500 nm	7	0.50 nm	0.644 nm

4.3.2 Binding state analyses (XPS results)

Co-doped TiO_2 system is widely investigated as a promising candidate for room-temperature ferromagnetic semiconductor, but the mechanism of magnetism in Co-doped TiO_2 remains controversial. The Y. Matsumoto group, which first reported the room-temperature ferromagnetic property of Co-doped TiO_2, suggests that the source of magnetism is from Co substitution for Ti in the lattice sites [1,3]. S.A. Chambers group also supports this idea based on their precise and detailed research [2,4,5]. On the other hand, other groups' work shows the existence of Co nano-clusters, which may be the origin of the ferromagnetic property. Thus, the binding state analysis is very important for the understanding of the mechanism for the incorporation of Co in $Co_xTi_{1-x}O_2$ systems.

4.3.2.1 Post annealing effect

In as-deposited samples, very thin Co layers or $Co_xTi_{1-x}O_2$ layers, which are all less than 10 Å, are inserted among TiO_2 layers. In this multilayer structure, post annealing is necessary to drive Co atoms to diffuse into TiO_2 layers, and substitute for Ti in the lattice sites. The annealing temperature is changed from 400°C to 600°C, while the annealing time is fixed at 1 hour.

In XPS spectra, we can identify different materials and their binding state according to the characteristic line position. For Co, 2p3 peak is the most common for use.

The standard values of Co 2p3 in different binding states are shown in the following:

*Ref: [16] **Ref.: [17]

bulk Co $\Rightarrow$ Co (0)	(778.3 eV)*	
$Co_3O_4 \Rightarrow$ Co(Ⅱ) + 2Co(Ⅲ)	(779.5 eV)*	antiferromagnetic **
CoO $\Rightarrow$ Co(Ⅱ)	(780.2 eV)*	antiferromagnetic **
$CoTiO_2 \Rightarrow$ Co(Ⅱ)	(780.2 eV)*	low spin state

Based on the XPS Co2p narrow scan patterns, Co oxidation state is found in most of samples with annealing temperature higher than 500°C (see Fig.4.2), and the center of Co

2p3 peak is nearest to 780.2 eV, Co(Ⅱ) oxide state. For 600°C annealed samples, Co(Ⅱ) peak is very obvious. From XPS patterns, we find that $Co2p^3$ peak is at about 780 eV and its intensity drops to the background level before 778.3 eV (neutral Co state). It indicates that Co in annealed samples is in oxide state and Co nano-cluster may not exist.

Fig.4.2 shows the annealing temperature dependant property of samples. Those samples have partial co-sputtering structure and fixed Co concentration at 5.62 at%. With the increase of annealing temperature, the intensity of Co(Ⅱ) peak increases. It is proved that post-annealing is an efficient way to drive Co atoms to diffuse into TiO_2 layers and substitute for Ti in the lattice.

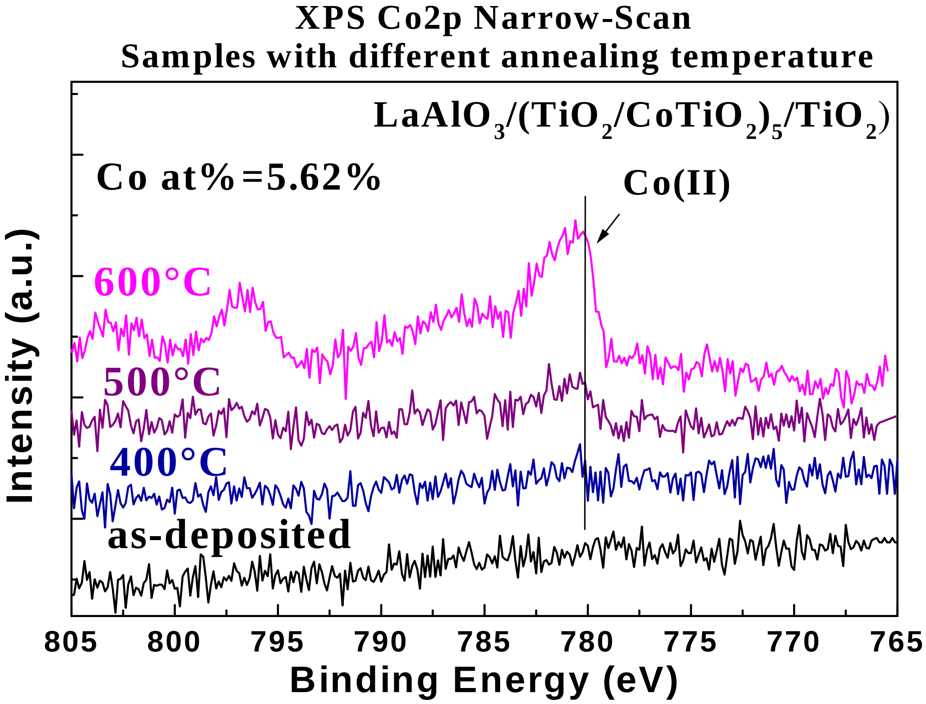

Fig. 4.2 Annealing temperature effect of $Co_xTi_{1-x}O_2$ films with partial co-sputtering structure. Co concentration is fixed at 5.62 at%.

4.3.2.2 Layer structure dependent property

Two kinds of samples with different layer structure are compared for post-annealing effect. They are partial co-sputtering structure (substrate/$(TiO_2/Co_xTi_{1-x}O_2)_n/TiO_2$) and pure multilayer structure (substrate/$(TiO_2/Co)_n/TiO_2$). From Fig.4.3, we can find that after annealing, partial co-sputtered samples have much stronger Co(II) 2p peak than those of multilayered samples. It indicates that post annealing treatment is much efficient for partial co-sputtering structure.

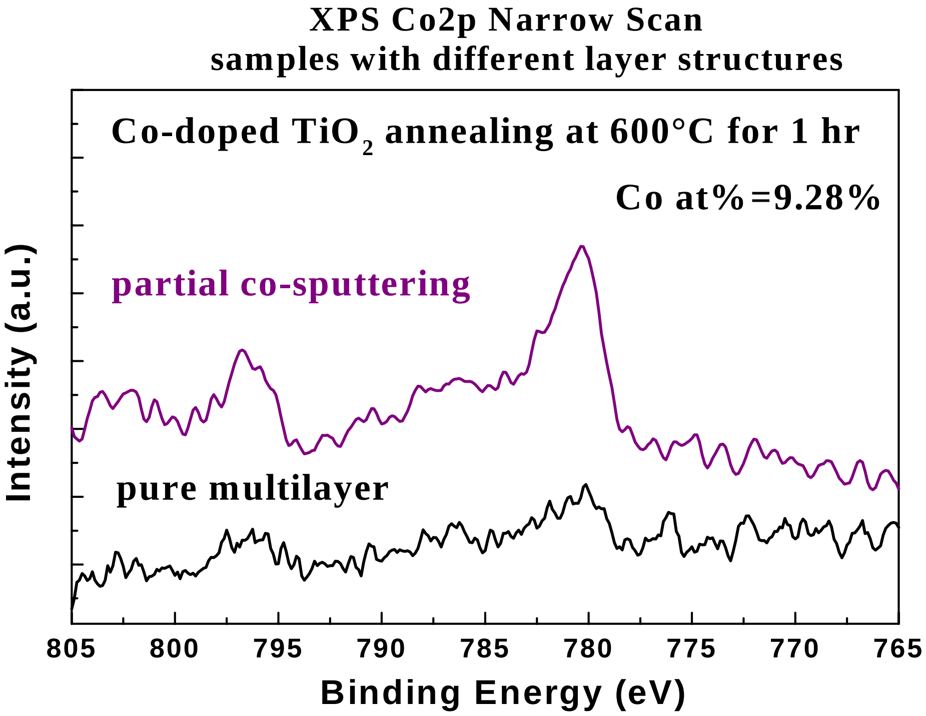

Fig.4.3 Layer structure dependant property of annealed Co-doped TiO_2 films. Samples with partial co-sputtering structure have much stronger Co(II) $2p^3$ peak than those of pure multilayer structure.

In 4.3.1, we have calculated the thickness of each layer of as-deposited samples based on ICP results. The inserted Co layer or $CoTiO_2$ layer between TiO_2 layers are all very thin, most of them are about 0.5 nm. The partial co-sputtering structure with inserted $CoTiO_2$

layer has much stronger Co(Ⅱ) $2p^3$ peak than pure multilayer structure, which inserts Co layer into TiO_2 layers. There are two possible reasons for this phenomenon. One is the defect induced by the co-sputtering process, such as vacancies. This kind of vacancies will function as channels for Co atoms to diffuse into TiO_2 matrix during the annealing process. That facilitates the substitution of Co for Ti in the lattice sites in the co-sputtered structure. The other reason may be the difference of the diffusion length needed for Co to replace Ti. For Co layer structure, there are about 3~5 atomic layers in the inserted layers. The Co atoms in the interface of Co and TiO_2 layers are easy to interact with Ti in the lattice, while the Co atoms in the middle layers have relatively long distance to diffuse in order to substitute Ti. For $CoTiO_2$ co-sputtering structure, Co atoms are mixed with TiO_2 so that the diffusion length needed to Co atoms is short.

4.3.2.3 In-depth analysis

To further prove the existence of Co(Ⅱ) state in annealed samples, more XPS experiments have been done with different sampling depth. Except for scanning in the surface of samples (as-received state), we also sampled in the depth of 0.9 nm and 1.8 nm, respectively. Before the deep scanning, pre-sputtering process is needed to reach required depth. In the XPS experiments, the pre-sputtering rate is calibrated by SiO_2.

Fig.4.4 shows the XPS patterns of the same annealed samples with different sampling depth. This sample has partial co-sputtering structure and Co concentration is 9.28 at%. In as-received state without pre-sputtering, Co peak is about 780 eV, and its intensity return to background level in around 778.3 eV, which is the standard binding energy of neutral Co. When increasing the sampling depth, Co peak shifts gradually to the low binding energy side. The same trend of Co peak shifting is found in all annealed co-sputtering samples. This phenomenon may be related to the pre-sputtering process employed before the deep scanning. During the preferential sputtering, oxygen is removed from the matrix material at a faster rate than some metallic elements, such as Co and Ti. The bonding between Co and O may be broken, and Co will lose the surrounding O. Thus Co(Ⅱ) is easy to become neutral Co after pre-sputtering. The shifting of Co peak after pre-sputtering just indicates that there is another binding state of Co in annealed samples other than neutral Co.

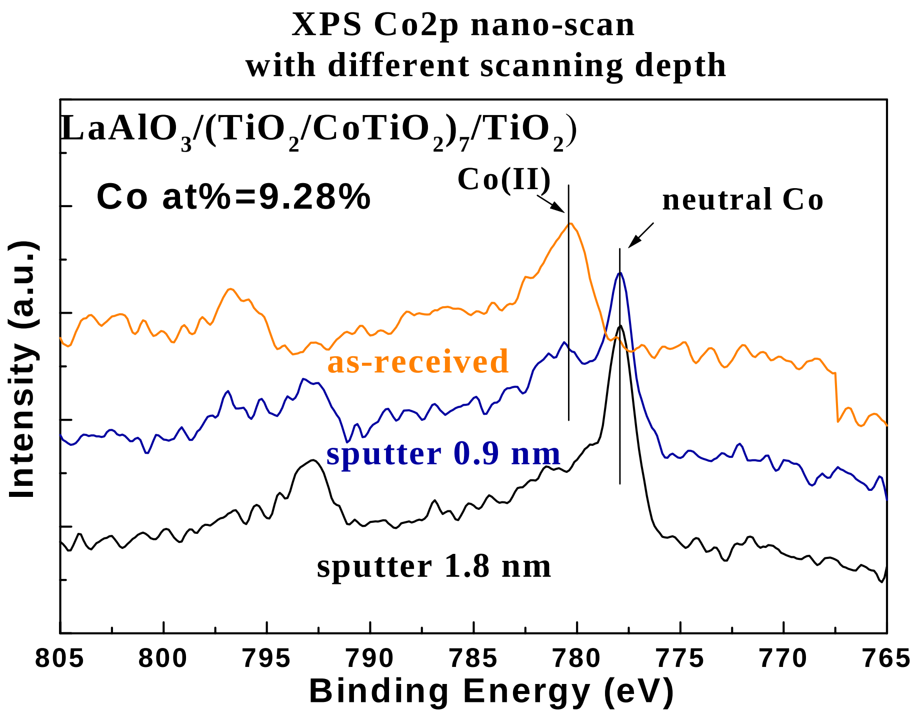

Fig.4.4 XPS patterns with different sampling depth of the same annealed sample, which has partial co-sputtering structure and 9.28% Co at%. The shifting of Co peak after pre-sputtering just indicates the existence of another binding state of Co other than neutral state.

Fig.4.5 is the XPS patterns of pure multilayer structure sample with different sampling depth. The intensity of Co peak is very weak, comparing with the patterns of co-sputtering samples.

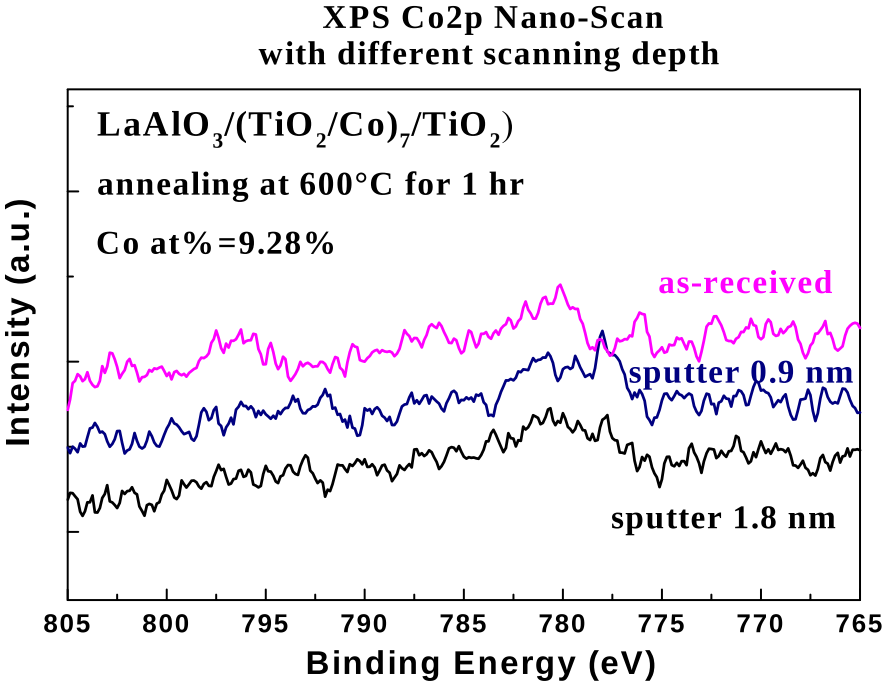

Fig. 4.5 XPS patterns of pure multilayer sample with different sampling depth. Sample was annealed at 600°C for 1 hr and has 9.28% Co at%.

The patterns of Ti 2p narrow scan also show the change of Ti binding state. From Fig.4.6, we find that the shoulder of Ti peak appears after pre-sputtering. The intensity of the Ti peak shoulder increases with the sampling depth (sputtering time). The reason is the same as that of the shifting of Co peak. Ti loses its surrounding O, and partially changes from Ti (Ⅳ) to neutral Ti state. Thus the shoulder is due to the combination of Ti (Ⅳ) and neutral Ti peak. Because of the great amount of Ti ions in the thin film, Ti (Ⅳ) peak still exists.

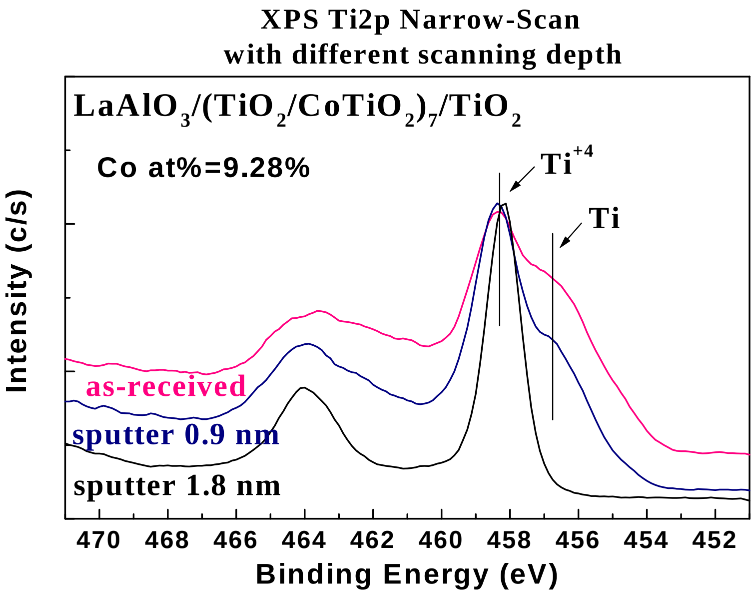

Fig. 4.6 XPS narrow scan patterns of Ti 2p peak with different sampling depth. The shoulder of Ti peak appears after pre-sputtering process, which indicates the change of Ti binding state from Ti(Ⅳ) to neutral Ti state.

There may exist another possible reason for the chemical shift of Co peak. It is the formation of Co in the surface area, while keep neutral state inside of annealed samples. This assumption contradicts some of the experimental results. In TEM-SAD patterns, we cannot find any Co oxide phase in annealed samples. And according to this assumption, Co will be in neutral state inside the annealed samples. So M_s will be in the range between the values of Co(II) (1.1~1.3 u_B/Co) and Co(0) (1.7 u_B/Co). But VSM data (1.24 u_B/Co) shows that it is much near to the value of Co(II) state. Finally, neutral Ti state also appears in the depth-scan. A shoulder exists near Ti(Ⅳ) peak, which means that the Ti 2p3 peak is the combination of Ti(Ⅳ) and Ti(0). If pre-sputtering treatment is not the reason for the formation of elemental Ti, Ti(0) phase should be detected by TEM. Thus, though we cannot exclude the second assumption, the possibility of it is small.

4.3.2.4 Co concentration effect

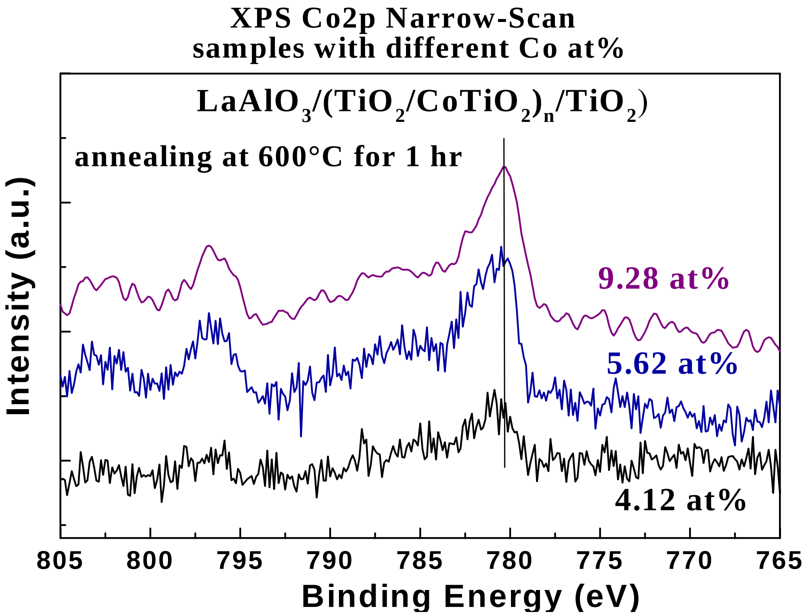

Fig. 4.7 XPS patterns of samples with different Co concentration.

As shown in Fig.4.7, Co binding state is same in annealed samples with different Co concentration, and the intensity of Co peak is increasing with the Co concentration.

4.3.3 Microstructure analysis (TEM result)

The selected-area diffraction pattern of TEM is shown in Fig. 4.8. The sample with partial co-sputtering structure was annealed at 600°C for 1 hour. Rutile-TiO_2 phase is the dominant phase in the annealed samples, and films have polycrystalline structure. Anatase-TiO_2 phase with (008) direction is found. Anatase-TiO_2 (211), (404) may exist, which is close to those of rutile-TiO_2 phase. From TEM-SAD patterns, Co-fcc phase is not found in annealed films. Because Co-hcp (100), (200) are very close to rutile-TiO_2 (111) and (330), respectively, Co-hcp phase cannot be excluded just based on TEM results.

4.3.4 Magnetic property analysis (VSM and AGM result)

In as-deposited state, samples show almost non-magnetic property. After annealing, samples at room-temperature show ferromagnetic characters. With the increase of annealing temperature, saturation magnetization (M_s) increases. Especially after annealed at 600 °C for 1 hour, M_s has a big jump and reaches 1.24 u_B per Co atom at room-temperature (see Fig. 4.9).

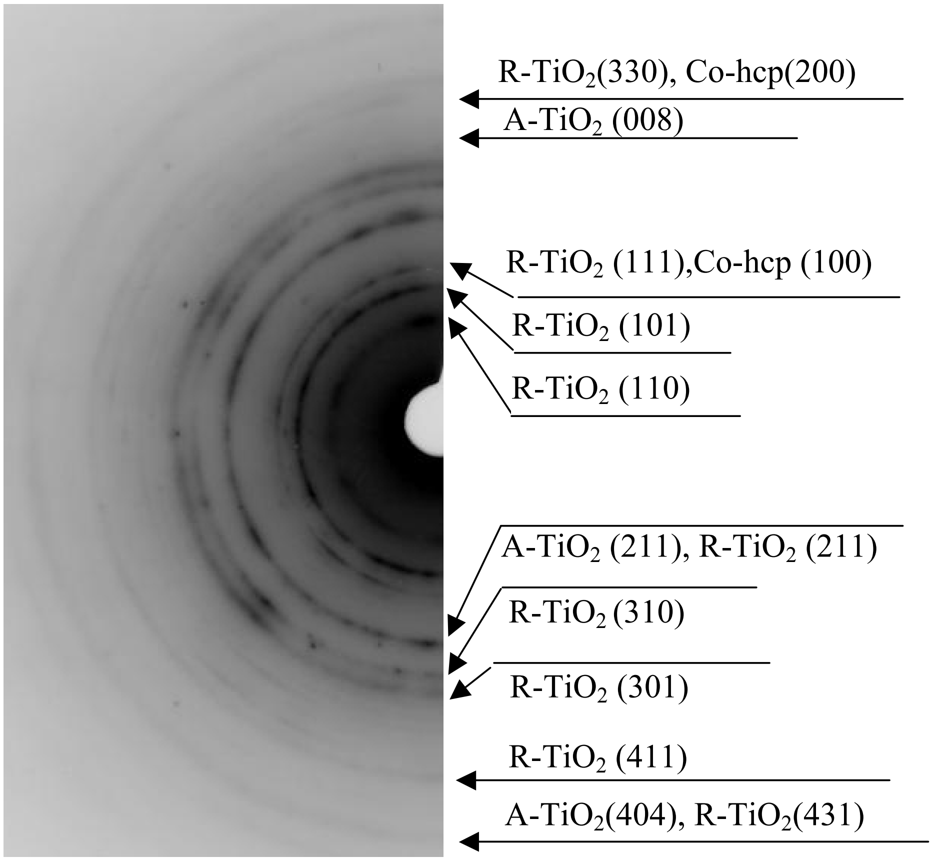

Fig. 4.8 TEM Selected-Area Diffraction pattern of annealed Co-doped samples. Rutile-TiO_2 phase is dominant in the film. Anatase-TiO_2 and Co-hcp may exist. And Co-fcc is not found.

Magnetic behavior of annealed samples at low-temperature was also investigated. Samples show obvious ferromagnetic behavior (see Fig.4.10). Sample with partial co-sputtering structure has M_s=1.325 u_B per Co atom at 150 K, after annealing at 600 °C for 1 hour. This value is close to the value of low-spin Co(Ⅱ) state [4].

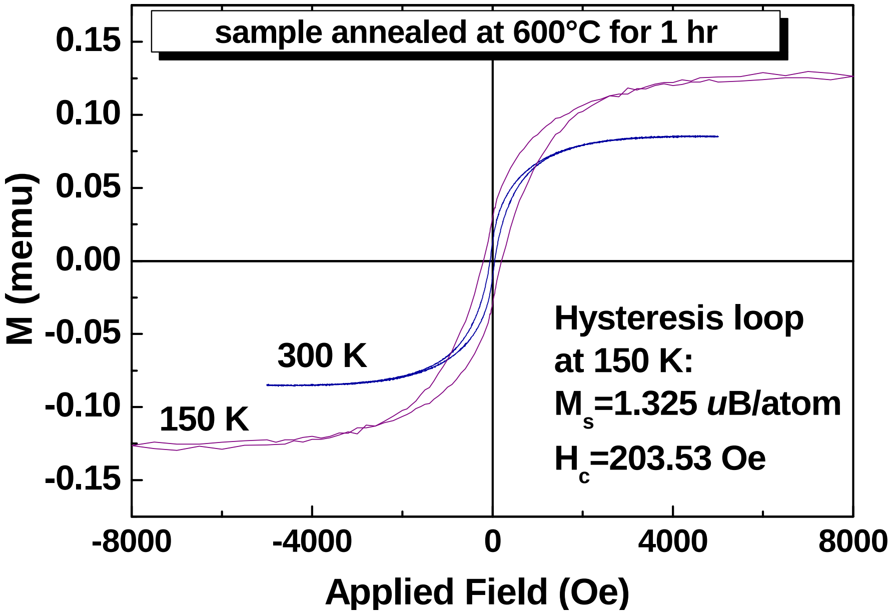

Fig.4.10 Low temperature (150 K) and room-temperature (300K) hysteresis loops of the same annealed sample with partial co-sputtering structure. M_s is 1.325 u_B per Co atom, which is close to the value of low-spin Co (Ⅱ) state.

In most of the literature, the magnetic property of Co-doped TiO_2 system is discussed by using the unit of (u_B/Co atom). Thus in order to keep our results comparable with theirs, we transfer the unit from memu/cm^3 (from experiment data) to u_B/Co atom by calculation. The detailed calculation has the following procedures.

$1\text{emu} = 4\pi u O_e = 1.0783*10^{20}\ u_B$

$V_{Co}=S_{film}*t_{film}$

$N_{Co}= (V_{Co}*N_A)/\rho_{Co}$

Where, S_{film}: area of thin film; t_{film}: thickness of thin film;

N_{Co}: the number of Co atoms; N_A: Avogadro constant $=6.02*10^{23}$ mol^{-1};

ρ_{Co}: the density of Co=58.933g/cm^3

Thus: 1 emu/cm^3=$(1.0783*10^{20}\ u_B *N_A*V_{Co})/\ \rho_{Co}$

4.4 Summary

We have investigated Co-doped TiO_2 thin films with different layer structures and Co concentration. Post annealing treatment has been done in order to enhance the diffusion of Co atoms into TiO_2 matrix. The binding states of Co and Ti in thin films, the microstructure and magnetic property of Co-doped TiO_2 films have been investigated in detail. Based on XPS Co 2p narrow scan patterns, Co(Ⅱ) binding state is found in most annealed samples, and its intensity increases with the annealing temperature. It is proved that post-annealing is an efficient way to drive Co atoms to diffuse into TiO_2 layers and substitute Ti in the lattice. It is very interesting to find that samples with partial co-sputtering structure have much stronger Co(Ⅱ) peak than those of multilayer structure. When increasing the sampling depth, Co peak shifts gradually to the low binding energy side. This shifting after pre-sputtering just indicates that there is another binding state of Co in annealed samples other than neutral Co. TEM-SAD patterns show that the annealed films have poly-crystal rutile-TiO_2 phase. Co-fcc phase is not found in annealed films. Anatase-TiO_2 and Co-hcp phase may exist. The low-temperature VSM measurement shows the saturation magnetization at 150 K is 1.325 u_B per Co atom, which is close to the value expected for low-spin Co (Ⅱ).

Reference:

[1] Y. Matsumoto, M. Murakami, T. Shono et al., *Science* **291**, 854 (2001)

[2] S.A. Chambers, S. Thevuthasan, et al., *Appl. Phys. Lett.* **79**, 3467 (2001)

[3] Y. Matsumoto, M. Murakami, T. Hasegawa, et al., *Appl. Surf. Sci.* **189**, 344 (2002)

[4] S.A. Chambers, T. Droubay, C.M. Wang, et al., *Appl. Phys. Lett*. **82**, 1257 (2003)

[5] S. A. Chambers, S. M. Heald, and T. Droubay, *Phys. Rev. B* **67**, 100401® (2003)

[6] Y. Matsumoto, M. Murakami, Z. Jin, et. al, *Jpn. J. Appl. Phys*. **38**, L603 (1999)

[7] W.K. Park, R.J. Ortega-Hertogs, J.S. Moodera, A. Punnoose, and M.S. Seehra, *J. Appl. Phys*. **91**, 8093 (2002)

[8] B.Z. Rameev, F. Yildiz, L.R. Tagirov, B. Aktas, et. al, *J. Magn. Magn. Mater*. **258-259**, 361 (2003)

[9] P.A Stampe, R.J. Kennedy, Y. Xin, J.S. Parker, *J. Appl. Phys*. **92**, 7114 (2002)

[10] D.H. Kim, J.S. Yang, K.W. Lee, S.D. Bu, et al., *Appl. Phys. Lett*. **81**, 2421 (2002)

[11] J.S. Yang, D.H. Kim, S.D. Bu, T.W. Noh, et al., *Appl. Phys. Lett*. **82**, 3080 (2003)

[12] J.-Y. Kim, J.-H. Park, B.-G. Park, et al., *Phys. Rev. Lett*. **90**, 017401-1 (2003)

[13] Y.L. Soo, G. Kioseoglou, S. Kim, Y.H. Kao, et al., *Appl. Phys. Lett*. **81**, 655 (2002)

[14] I.-B. Shim, S.-Y. An, C.S. Kim, S.-Y. Choi, Y.W. Park, *J. Appl. Phys*. **91**, 7914 (2002)

[15] S.A. Chambers, *Mat. Today* **5**, 34 (2002)

[16] S.A. Chambers, C.M. Wang, S. Thevuthasan, T. Droubay, et al., *Thin Solid Films* **418**, 197 (2002)

[17] "NIST SRD 20 Database of XPS Binding Energies", NIST: National Institute Standards and Technology.

[18] W. Kundig, M. Kobelt, H. Appel, et al. *J. Phys. Chem. Solids* **30** (1969) 819.

Chapter 5 Conclusion

New magnetic materials with high performance are needed to meet the increasing requirements of novel applications on data storage and spintronics. In this work, two kinds of new magnetic materials were investigated systematically. One was CoZr system for the application of patterned recording media and the other is Co-doped TiO_2 system as one of promising candidates for room-temperature ferromagnetic semiconductor.

5.1 CoZr system

$Co_{1-x}Zr_x$ sputtered thin films have been investigated in the first part of the work. Thermo-magnetic properties of films were analyzed in detail, which is important for the application of phase transition method to fabricate patterned nanostructures. The as-deposited samples change from non-magnetic state to soft-magnetic state, when increasing Co content. Post annealing treatment can effectively induce the phase transition of thin films from non-magnetic state to magnetic state, which results in the enhancement of M_s. Under the same annealing conditions (550°C, 2 hours), samples with 60% Zr at% have the most dramatic increase in M_s. It is interesting to find that the annealing temperature needed for phase change in our samples is much lower than that of rapidly quenched bulk samples. $Co_{11}Zr_2$ and $Co_{23}Zr_6$ magnetic phases are formed after annealing, which may lead to the enhancement of the magnetism of annealed samples. The calculations on TEM-SAD patterns also show that the enlarged grain size may be another source of the magnetic enhancement. The M_s of these two phases were calculated based on the TMA data. They are 1066 emu/cm^3 and 924 emu/cm^3, respectively. When increasing the annealing time at fixed annealing temperature, M_s increases continuously, while H_c of out-of-plane has the maximum value after 5~8 hours annealing. In all annealed samples, perpendicular magnetic anisotropy is revealed.

5.2 Co-doped TiO_2 system

In the second part of this work, Co-doped TiO_2 thin films were studied by changing layer structures, Co concentration, and post-annealing conditions. XPS analysis on binding states of Co and Ti atoms in thin films were reported for the first time for this system. Based on XPS Co2p narrow scan patterns, Co(Ⅱ) binding state is found in most annealed samples, and its intensity increases with the annealing temperature. It is proved that post-annealing is an efficient way to drive Co atoms to diffuse into TiO_2 layers and substitute for Ti in the lattice. In order to investigate the behavior of Co atoms during the annealing, two different layer structures were designed. It is very interesting to find that samples with partial co-sputtering structure have much stronger Co(Ⅱ) peak than those of multilayer structure. In the in-depth analysis, Co peak shifts continuously to the low binding energy side when increasing the sampling depth. This kind of shift of Co peak after pre-sputtering indicates that there exists another binding state of Co in annealed samples other than neutral Co state. TEM-SAD patterns show that the annealed films have polycrystalline rutile-TiO_2 phase. Co-fcc phase is not found in annealed films. The low-temperature VSM measurement shows the saturation magnetization at 150 K is 1.325 u_B per Co atom, which is close to the value expected for low-spin Co(Ⅱ).

PUBLICATIONS

1. J.L. Xu, **Xiaofeng Yao** and J.Y. Feng, “The Influence of the vacuum annealing process on electrodeposited $CuInSe_2$ films”, S*ol. Energy Mater. Sol. Cells*, 73 (2002) 203-208.

2. **Xiaofeng Yao**, J.P. Wang, T.J. Zhou, T.C. Chong, “Microstructure and Magnetic Properties of CoZr Thin Film”, *J. Appl. Phys.*, 93 (2003) 8310-8312.

3. Y. Zhao, T.J. Zhou, J.P. Wang, **Xiaofeng Yao**, et. al, “Submicro Co(TaC) line array produced by electron-beam direct writing”, *J. Appl. Phys.* , 93 (2003) 7417-7419.

4. **Xiaofeng Yao**, T.J. Zhou, Y.X. Gai, J.P. Wang, C.T. Chong, “Binding State and Microstructure Analyses of Co-doped TiO_2 Thin Film”, *the 9th Joint MMM-Intermag Conference*, in process, June. 2004.

CONFERENCES

Xiaofeng Yao, J.P. Wang, T.J. Zhou, T.C. Chong, “Microstructure and magnetic properties of CoZr thin film”, 47th Annual Conference on Magnetism & Magnetic Materials, November 11th – 15th, Tampa, Florida, 2002.

Xiaofeng Yao, T.J. Zhou, Y.X. Gai, J.P.Wang, T.C. Chong, “Binding state and microstructure analyses of Co-doped TiO_2 thin film”, 9th Joint Conference of MMM & Intermag, January 5th-9th, Anaheim, California, 2004.